1972

An experimental investigation of an incompressible wall jet impinging on a receiver with spill port

Stephen John Bach
Lehigh University

AN EXPERIMENTAL INVESTIGATION OF AN INCOMPRESSIBLE WALL JET IMPINGING ON A RECEIVER WITH SPILL PORT

by

Stephen John Bach

Abstract

A wall jet impinging on a receiver with a spill port located at 90° with respect to the wall jet was investigated. The effects of receiver width and length on the flow field were studied for a range of downstream loading conditions varying from fully opened to completely blocked. Velocity profiles, wall static, and total pressure measurements were taken. It was found that the static pressure recovery coefficient increased with increasing spill flow up to the point at which the jet switches to the spill port side of the receiver. The switching occurs at lower spill flow ratios for the larger setback cases.

AN EXPERIMENTAL INVESTIGATION OF AN INCOMPRESSIBLE WALL JET IMPINGING ON A RECEIVER WITH SPILL PORT

by

Stephen John Bach

A Thesis
Presented to the Graduate Committee
of Lehigh University
in Candidacy for the Degree of
Master of Science
in
Mechanical Engineering

Lehigh University

1972

This thesis is accepted and approved in partial fulfillment of the requirements for the degree of Master of Science

September 8, 1972
(date)

Harold O. Rothschild
Professor in charge

Frederick T. Adler
Chairman of the Department

Acknowledgements

The author wishes to express his gratitude to Dr. Donald O. Rockwell, whose guidance and encouragement accompanied the entire work.

He also wishes to thank his wife, Karen, for her patience and encouragement while typing this manuscript.

Table of Contents

List of Figures

Abstract

A wall jet impinging on a receiver with a spill port located at 90° with respect to the wall jet was investigated. The effects of receiver width and length on the flow field were studied for a range of downstream loading conditions varying from fully opened to completely blocked. Velocity profiles, wall static, and total pressure measurements were taken. It was found that the static pressure recovery coefficient increased with increasing spill flow up to the point at which the jet switches to the spill port side of the receiver. The switching occurs at lower spill flow ratios for the larger setback cases.

Nomenclature

C	control port width
C_p	pressure recovery coefficient $\frac{P - P_C + \Delta P_N}{1/2\ \rho\ \bar{V}_t 2}$
H	height of nozzle
L	length of receiver channel
P	static pressure at point of interest
$\mathbb{P}$	total pressure coefficient
P_C	static pressure upstream of the contraction in the nozzle
P_t	static pressure measured at the throat
P_T	total pressure at a given location
P_{20}	static pressure at Tap 20
ΔP_N	reference pressure drop through the nozzle contraction (P_C - P_t) measured at zero spill flow ratio
ρ	density
Q_i	inlet flow (cfm)
Q_o	outlet flow (cfm)
Q_s	spill flow, Q_i - Q_o, (cfm)
Q_s/Q_i	spill flow ratio
S	distance of setback
S/W	setback ratio
u	velocity at point under consideration
U_M	maximum velocity for each individual spill flow

$\bar{V}_t$	average velocity at nozzle throat
W	width of nozzle
X	distance measured downstream from nozzle exit
Y	distance measured across width of nozzle
Z	distance measured between parallel bounding walls of test section

1. Introduction

In fluid amplifiers, a jet exits from a supply nozzle and impinges upon one or more of the downstream receivers. At times the flow out of the receiver can become partially or totally impeded. If this receiver exit loading does occur, some of the flow spills into another receiver leg or into a vent. In the cases of bistable and proportional amplifiers, one output port can function as the active receiver, and some flow may spill into the inactive receiver and/or the vent, depending on the geometry. In the instance of the proportional amplifier, where the vents are often as long as the receivers, the vents themselves may experience downstream loading. In this event, some of the vent flow may be spilled into one of the other available ports.

The related problem of turbulent jet mixing in an axisymmetric duct is described by Hill (1).* For the case of a jet entering a constant velocity stream and subsequently mixing in the duct, a theory is developed from moment of momentum integral equations. The theory employs previously obtained free jet data. By using the assumption that the flow is self-preserving, it is possible to predict velocity profiles. With the addition of the following assumptions: no recirculation zone, negligible influence of

*numbers in parentheses refer to corresponding numbers in the bibliography

the wall boundary layers, and potential outer flow until the jet attaches, it is possible to predict the velocity fields in a duct.

These theoretical predictions are checked with experimental data. A six-inch diameter duct with a nozzle-to-duct diameter of 0.10 provided wall pressure distributions. Wall pressure recovery was plotted. At the lower mass flow ratios (jet to mainstream), the recovery decreases until approximately $X/D = 2$, after which follows an increase in the recovery to $X/D = 3$, the increase in the recovery is followed by a leveling trend. The pressure recovery coefficient increases from -0.05 to +0.5 for a unit change in X/D. For the higher mass flow ratios, the gradient of the pressure recovery curves decreases, at times, not leveling out until $X/D = 8$. The magnitude of the rise decreases with increased mass flow ratios, as does the magnitude of the wall pressure recovery. In a later work (2) Hill extends the theory to incompressible flow in a converging-diverging channel. Hickman, Hill, and Gilbert (3) expand Hill's original theory to include compressible effects in a converging-diverging channel. The aforementioned investigations apply only to ducts where all of the flow impinging on the duct passes through the duct. That is, none of the impinging flow is spilled.

Heskestad in his work (4) has studied the "edge suction effect". Flow was extracted from the mainstream which flowed over a 90° corner. Several applications of the "edge suction effect" are given, including step expansion in a pipe, right angle channel bend, and jet deflection. He reports that a two-dimensional jet has been deflected up to 45° by the use of edge suction at a suction rate (ratio of extracted flow to mainstream flow) of 3 percent.

Tillman and Sisto (5) carried Heskestad's work on jet deflection further. They investigated the effect of suction slot geometry on a free jet. An analytical model was obtained with the assumptions that the confining walls were represented by straight streamlines, and the boundaries of the jet are represented by free streamlines. The suction slot was modeled by a line sink located in the center of the slot. Mapping of the region was accomplished and the equations solved by a computer. Experiments were conducted on two different suction slot geometries. One, referred to as "0° slot angle", had the suction slot on the mainstream side of the confining wall. The other, called the "90° slot angle", had the suction slot on the perpendicular end face of the confining wall. Results showed, for the "0° slot angle", a decreasing jet deflection angle with increasing slot size for a fixed suction

rate. On the other hand, the "90° slot angle" showed increasing jet deflection for increasing slot size and constant suction flow. Experimental results corresponded well with the theoretical results for this potential flow model.

In later papers (6, 7), Heskestad reports on the axisymmetric flow into a sudden expansion to which suction is being applied at the corner of the expansion step. For this type of flow through an axisymmetric sudden expansion, the static pressure recovery is greatly increased. An expansion ratio of D_2/D_1 (diameter of the downstream section to diameter of the upstream section) of 1.93 was employed. For a Reynolds number of 1.03×10^5, based on the inlet pipe diameter, pressure recoveries are shown to increase from 0.4 to 0.8 with a suction flow of less than one tenth of the mainstream flow. Static pressure distributions along the wall downstream of the step are also plotted. Static pressure remains constant for a short distance (approximately $X/D_2 = 1$), after which it rises sharply then levels off (approximately $X/D_2 = 4$). The static pressure coefficient rises from zero to 0.4. When a small amount of suction is applied ($Q_s/Q_m = 0.061$ ratio of the spilled flow to the main flow), the rise in static pressure occurs at a shorter downstream distance (approximately $X/D_2 = 0.5$). The static pressure coefficient now rises from 0.6 to 0.8. The amount of recovery is shown to be considerably less

in the second instance; however, the magnitude of static pressure recovery in the downstream channel is much greater. A few tests are conducted with larger expansion ratios. The same trends are noted for these larger expansion ratios, although the magnitudes of the static pressure recoveries are not as high for comparable suction flows.

Experiments were also conducted with different widths of the suction port. Total pressure, static pressure, and velocity profiles were taken for different suction slot widths. Pressure recovery coefficients were plotted versus Q_s/Q_m. As the slot width (a/D_1, a "projection of suction gap normal to approach leg of corner") was increased, the rise in pressure recovery previously mentioned occurs at higher and higher suction flows.

The preceding paragraphs give a brief review of what has been done previously. Except for Tillman and Sisto, all of the previous works were axisymmetric. All of the aforementioned works took into consideration symmetric geometries; i.e., suction ports located on both sides of the two-dimensional nozzle, or circumferentially around the duct. In the present work, a planar jet is considered. Unlike the other works, a wall jet, instead of a free jet, is studied. Contrary to previous investigations, an asymmetric geometry (only one wall is set back) and an asymmetric spill port are investigated. The spill

port acts as a relief vent for the various loadings.

The purpose of the present investigation is to study the effects of receiver length, receiver width, and amount of spilled flow on the wall jet receiver performance. In order to study the effects of downstream loading on a receiver, a simplified model was constructed. The model consists of a jet partially filling a single receiver (parallel channel) with a control port immediately downstream of the nozzle exit. From this model, static pressure recovery, contours of constant total pressure, and velocity fields can be obtained for the receiver channel. Two different receiver lengths were tested. Three different receiver widths at each of the receiver lengths were examined. For these six cases, the flow was spilled in increments of one tenth of the main flow from zero percent spillage to one hundred percent spill flow (receiver completely blocked). The flow which did not pass through the receiver was spilled at a right angle to the main jet flow. Total pressure measurements were taken at the exit of each receiver (upstream profiles were taken in only one case). Wall static pressure measurements were taken on both sides of the receiver throughout the entire receiver length.

2. Experimental Apparatus

An overall view of the experimental system is sketched in Figure 1. The main test rig was elevated on wooden struts as shown. These struts had no effect other than to make assembly and disassembly of the test rig easier.

The flow systems upstream and downstream of the test section are shown in Figure 2. Air was pumped through an air dryer into a stagnation tank. The tank was maintained at a constant pressure of 65 psig. From the stagnation tank, the air flowed through a pressure regulator (Moore Products pressure regulator Model 42H30), which was preceded and followed by a needle valve. At the next station downstream, the flow was measured by a calibrated Venturi meter. Each Venturi meter was calibrated separately then recalibrated in tandem to insure accurate calibration curves. The curves are shown in Figure 3. The flow then passed through the main test section. Downstream of the test section was located another calibrated Venturi meter to measure the outlet flow. Flow straighteners and/or screens preceded each of the Venturi meters to insure uniform inlet flow conditions and, consequently, accurate flow measurement. (The flow straighteners were a plastic material with $1/8$" honeycomb cell parallel to the direction of flow.) By knowing accurately the outlet and inlet

flow, the spill flow ratio $Q_s/Q_i = \frac{Q_i - Q_o}{Q_i}$ could be determined. Since determination of the spill flow ratio was done indirectly, it was necessary to insure no leaks were occurring anywhere in the system. The system was sealed with vacuum grease (Fisher Scientific Co. Vacuum Grease, silicone lubricant 14-635-5) and checked for leaks before any data was taken. A valve was placed after the second Venturi meter to allow variation of the back pressure and, therefore, the spill flow rate. The air that passed through the test section and outlet Venturi meter was exhausted to the atmosphere.

The test rig itself was made of plexiglas. Schematics of the test section are shown in Figures 4-7. Pictures of the actual apparatus are shown in Figure 8. The nozzle, the receiver, and the plenum chamber were sandwiched between parallel side walls. One parallel side wall was $1/2$" thick and contained the mountings for the Z direction total pressure traverse. The other parallel side wall was $3/4$" thick and served as the base plate. All of the other pieces (e.g. nozzle, receiver, and plenum) were bolted to this side plate. The pieces sandwiched in between the parallel side walls were machined to 2.00 ± 0.005 inches. The nozzle had a contraction ratio of 6.52 to 1. The nozzle flow straightener was located upstream of the

nozzle contraction after the perpendicular inlet. The nozzle consisted of a concave portion, followed by a straight section, leading into a convex portion. The convex portion was followed by a short ($^1/_4$") straight section. The spill port side of the nozzle (side A) ended abruptly after the $^1/4$" straight section of the nozzle, dropping off at 90° to form one wall of the spill port. The spill port side of the nozzle was movable, which allowed the aspect ratio to be changed if desired. When the nozzle was being used, the nozzle exit had dimensions of $^1/4$" by 2", or an aspect ratio of 8. This aspect ratio was kept constant throughout the test program. The wall jet side (continuous extension) of the nozzle (side B) was fixed. This side of the nozzle was continuous throughout the length of the receiver for all different receiver lengths. The discontinuous side of the receiver formed the other side of the spill port. The spill port was $^1/4$" wide extending from one parallel side wall to the other. A sliding gate was devised so that the spill port could be partially or totally blocked. The discontinuous wall was parallel to the continuous wall and reached as far downstream as the continuous wall. Two different lengths of discontinuous wall were tested: 6W and 30W (where W is the width of the nozzle). The continuous and discontinuous walls, for each discontinuous wall

length tested, always ended at the same downstream location. Each discontinuous wall could be moved to setbacks of 0W, 1W, 2W (e.g. channel widths of 1W, 2W, 3W). The continuous wall had static pressure taps at the following locations: (1) one tap before the contraction in the nozzle; (2) one tap at the throat of the nozzle; (3) taps starting at 2W downstream of the throat, separated by 1W, until 11W downstream of the throat; then taps separated by 2W intervals until the end of the receiver. In the case of the short receiver (length = 6W), all of the taps were 1W apart. The discontinuous wall had static pressure taps placed at the same locations as in the continuous wall; however, due to the spill port, the nearest tap to the nozzle throat was located at a downstream distance of 3W. After the receiver, the flow exited into a plenum chamber. The walls of the plenum chamber were fixed in place far away from the receiver walls. The ratio of the plenum cross sectional area to the receiver exit area varied from 8.7 to 26, depending on the value of setback of the discontinuous wall. The x distance from receiver exit to plenum end wall varied according to receiver length (i.e., plenum was 24W longer when 6W wall was being used). A flow straightener was placed in the plenum a constant distance of one inch from the receiver exit.

One of the plenum chamber walls had a hole to allow insertion of a total pressure probe at the exit of each receiver. The probe that passed through this hole was aligned along the midplane of the receiver. With this probe, a traverse could be taken from one side of the receiver exit to the other along the midplane. The probe that passed through the mounting on the parallel side plate was used to take Z direction traverses. (See Figure 9 for coordinate directions.) The angle of attack of this probe could be varied; and for the OW discontinuous wall setback, it was possible to cover the entire receiver exit area.

Each total pressure probe was locked into a traversing mechanism (Figure 10). The mechanism held the probe in a piece of plexiglas which was moved along a track by a lead screw. As the probe was traversed, distance was recorded on an X-Y plotter (EAI Variplotter 1110) by using a position transducer (Bourns Model PN 2001782009, Range 2.00 inches, potentiometer). Continuous total pressure readings were fed through a pressure transducer and plotted on the Y axis.

3. Experimental Procedure

Static pressure and midplane total pressure traverses were taken for all cases studied. Total pressure traverses in the Z direction could be taken only for the OW setback case. In the case of the long wall, two inclined manometers were used to take the static pressure measurements. One of the manometers, containing Meriam red oil, specific gravity 0.827, recorded the discontinuous wall static pressures. The continuous wall static pressure data were taken using water as the fluid in the manometer. Both manometers were inclined at 30° to the horizontal. For the case of the shorter wall, only the water manometer was needed. During each test the sump reference pressure in the manometer was the pressure upstream of the contraction P_c.

The total pressure probe was connected to a pressure transducer (Statham 1820 PL283TC) which was linear up to 9 inches of water impact pressure. The signal was then amplified and plotted versus distance (Y or Z, depending on the direction of the traverse) on the X-Y recorder. It was necessary to bias the pressure transducer because of the high system pressure. Static pressure Tap No. 20, the last tap on the continuous wall, provided the biasing pressure.

None of the data were taken until the discontinu-

ous wall had been placed and exact channel width measurements were taken with a telescopic micrometer. This telescope permitted measurements within 0.001 inch to be taken. All dimensions were accurate within a deviation of $\pm$0.004 inch. First, static pressure data for both walls were obtained for each spill flow. Next, midplane total pressure measurements were recorded. Only those spill flow ratios that produced discernible traces could be recorded. At higher spill flows, the dynamic pressure was either highly unsteady or so low in value that it could not be accurately transduced. All total pressure and velocity profiles were normalized with respect to the maximum value for the profile or series of profiles under consideration.

For the Z direction traverses, the probe tip was placed touching the base plate. With the telescopic micrometer, the Y distance from the continuous wall to the probe tip was measured. The probe was then traversed slightly past the midplane (Z = 0) and locked in place by the mounting chuck. The traversing mechanism had only a one-inch travel; consequently, the mechanism had to be returned to its starting point, the probe was then relocked into the traversing piece of plexiglas, and the mounting chuck lock released, in order to continue with the traverse. When the traverse was completed, the probe was returned to the starting position, and its angle of attack to the mainstream

was changed slightly to obtain a different Y value. The angle of attack never exceeded 15°. Z direction traverses were taken at Y locations verying by approximately 0.04 inches, thereby allowing the entire exit plane to be covered by the total pressure traverses. These Z direction traverses were taken for spill flow ratios of 0.1, 0.4, 0.6, and 0.8 for OW setback cases only. All of the data were taken at a Reynolds number based on the nozzle width of 2.5×10^4, which corresponds to a Mach number of 0.17.

4. Results and Discussions

From the velocity profile and the static pressure measurements, it is clear that the wall jet switches from the continuous wall at the higher value of setback ($^{S}/_{W} = 1$). At the lowest value of setback ($^{S}/_{W} = 0$), the velocity profiles indicate an increasing asymmetry with increases in spilled flow. Decreasing static pressure recovery with increasing spill flow for $^{S}/_{W} = 0$ also implies that switching of the jet occurs for higher spill flow. Figures 12 and 13 show the pressure recovery coefficient, C_p, at the exit of the receiver plotted versus $^{Q_S}/_{Q_i}$. The continuous wall data points are plotted as open symbols, and the discontinuous wall data points are plotted as filled symbols. When only a single symbol is shown, the data points for continuous and discontinuous wall are congruent. For the longest wall (Figure 12), the maximum exit pressure recovery coefficient is seen to shift from $^{Q_S}/_{Q_i} = 0.6$ for $^{S}/_{W} = 0$ to $^{Q_S}/_{Q_i} = 0.2$ for $^{S}/_{W} = 1$. The magnitude of the pressure recovery coefficient is greater for the $^{S}/_{W} = 1$ case. A negative pressure recovery coefficient indicates an accelerating flow in the receiver. The accelerating flow is possible for the $^{S}/_{W} = 0$ case, assuming the spill port acts as a localized disturbance for the lower spill flow ratios. That is, the remaining flow quickly fills the channel, and the wall boundary layer rapidly builds

up to produce an acceleration of the flow. Traverses in the Z direction, to be explained later, will show that the effect is indeed a local one restricted to a region within several $^{x}/_{w}$ downstream for the lower spill flow ratios. For the shortest wall (Figure 13), a shift is again seen in the maximum exit pressure recovery coefficient. This time the shift occurs from $^{Q_s}/_{Q_i}$ = 0.5 for $^{s}/_{w}$ = 0 to $^{Q_s}/_{Q_i}$ = 0.1 for $^{s}/_{w}$ = 1. Unlike the longest wall, the magnitude of the pressure recovery coefficient for the $^{s}/_{w}$ = 0 case is the larger of the two. In both cases, for the blocked load condition, $^{Q_s}/_{Q_i}$ = 1.0, the exit pressure recovery coefficient coincide for the different setbacks of each wall.

Figure 14 shows the average value of $\frac{(P_c - P_t)}{1/2\rho\bar{V}_t^2}$ indicates a decrease in $P_c - P_t$ for an increase in the spill flow ratio. The maximum decrease is approximately 15%. This variation of $\frac{(P_c - P_t)}{1/2\rho\bar{V}_t^2}$ is due to the high streamline curvature at the throat caused by the spilling of fluid out of the perpendicular exit. Due to the high streamline curvature, the static pressure is not constant across the nozzle throat. Therefore, instead of using the varying throat pressure as a reference pressure, a different reference is used. The new reference is taken as P_c which

remains constant for all spill flow ratios, plus a normalizing factor $P_c - P_t$ taken at a spill flow ratio of zero. This new factor allows the pressure to be indirectly referenced to the throat. The new pressure recovery coefficient becomes $C_p = \frac{P - P_c + \Delta P_N}{1/2\ \rho\ \bar{V}_t^2}$ where $\Delta P_N = (P_c - P_t)$ at $Q_s/Q_i = 0.0$

Figures 15 through 18 show the normalized Y direction velocity profiles obtained at the exits of the channels. For the longest wall, $s/w = 0$, the profiles are nearly similar with respect to varying spill flow. Even for the higher extraction ratios, due to the length of the channel, the asymmetry associated with the spill flow near the channel entrance is unnoticeable. Even though there is this nearly complete elimination of upstream history effects, Figure 15 shows the velocity profile peak to be shifted slightly toward the discontinuous side at the higher spill flow ratios. Q_s/Q_i of 0.4 shows the most pronounced shift toward the discontinuous wall. $Q_s/Q_i = 0.6$ shows the greatest deviation on the right-hand side. In the case of $s/w = 1$, Figure 16, a left-to-right shift can be seen most prominently for $Q_s/Q_i = 0.1$. This shift coincides approximately with the maximum on the exit pressure recovery coefficient graph at $Q_s/Q_i = 0.2$. The two previous graphs (15 and 16) showed that the maximum deviation from a symmetrical profile occurs just prior to the peak in the exit

pressure recovery coefficient which will be shown to correspond to the switching of the jet. In Figure 17, $^{s}/_{w} = 0$, for the shortest wall, the effect of the spill port is obvious. At zero spill flow ratio, the profile is almost symmetrical with respect to $^{Y}/_{W} = 0.5$. As the spill flow ratio is increased, more and more of the fluid is pulled away from the continuous wall, until, for the $^{Q_s}/_{Q_i} = 0.8$ case, the profile is similar to a wall jet with some entrained flow. In Figure 18, the jet switching effect is most noticeable. At zero spill flow ratio, the jet is seen to be attached to the continuous wall in the typical wall jet profile. For $^{Q_s}/_{Q_i} = 0.1$, the jet has already started to be drawn toward the discontinuous wall, and the velocity profile resembles a wall jet with a large entrained flow in the upper layer. The higher flows indicate that the wall jet has switched over to the discontinuous wall. From Figure 13, the shortest wall with $^{s}/_{w} = 1$ is shown to have a peak in the exit pressure recovery coefficient between $^{Q_s}/_{Q_i} = 0.1$ and $^{Q_s}/_{Q_i} = 0.2$. Considering simultaneously the velocity profile, it can be seen that the peak in the recovery coefficient coincides with the switching of the jet from the continuous wall to the discontinuous wall.

Figures 19 through 29 show the pressure recovery coefficient plotted versus $^{x}/_{w}$ for all of the spill flow ratios. The continuous wall data points are plotted as open symbols, and the discontinuous wall data points are

plotted as filled symbols. Figure 19 shows the longest wall at $S/W = 0$. For this case, all of the flows show an acceleration in the receiver channel. The $Q_S/Q_i = 0.0$ case has an accelerating flow throughout the receiver length as though the spill port slot were not present in the flow field. The case of $Q_S/Q_i = 0.1$ has a flat plateau for a short distance before the flow begins to accelerate down the length of the receiver. The spill port has only started to play a role in the shape of the pressure coefficient curve. The flow is greatly affected by the spill port in the $Q_S/Q_i = 0.2$ case. According to potential theory, there should be a separating streamline which ends at a stagnation point at the leading edge of the discontinuous wall. This streamline would divide the flow into the 20 percent that is spilled and the 80 percent that continues on. The continuing 80 percent would see a 25 percent increase in the channel width and would spread to fill the channel, causing an increase in the pressure recovery coefficient. As the spill flow is increased, less fluid must fill the same area downstream of the spill port; therefore, the fluid must decelerate to satisfy the continuity equation, and hence the pressure recovery coefficient increases. After the initial expansion takes place, the fluid sees a narrow parallel wall channel and starts to accelerate. Figure 20 shows the higher spill flow ratios for the longest wall $S/W = 0$. As the spill flow ratio is increased, the

peak in the pressure recovery coefficient is moved downstream of the throat: from $^{x}/_{w}$ = 3 to $^{x}/_{w}$ = 8. At $^{Q_s}/_{Q_i}$ = 0.6, the exit pressure recovery coefficient has reached a peak. After this point, with increasing spill flow ratio, the pressure recovery coefficient decreases, and no acceleration occurs in the receiver channel. For spill flow ratios greater than $^{Q_s}/_{Q_i}$ = 0.6, the flow seems to have reached a maximum recovery and seems to remain at this value. The continuous and discontinuous wall pressure recoveries for large ($^{x}/_{w}$ > 10) downstream distances agree extremely well, indicating the static pressure is approximately constant across the receiver channel. For smaller $^{x}/_{w}$ distances two distinct curves for each spill flow can be seen. This can be explained by streamline curvature in the entrace region of the receiver at the higher spill flow ratios. Figure 21 shows the effect of the setback on the flow. The acceleration in the receiver has been eliminated. Even for the zero spill flow case, the increased setback causes the flow to decelerate instead of accelerate. Once the spill port is opened, it has the same effect on the flow as the $^{s}/_{w}$ = 0 case: the pressure recovery coefficient increases until the jet switches to the discontinuous wall. The increased setback is unable to support the wall jet on the continuous wall after $^{Q_s}/_{Q_i}$ = 0.1. The jet switches between $^{Q_s}/_{Q_i}$ = 0.1 and $^{Q_s}/_{Q_i}$ = 0.2. For this

larger setback, the switching is immediately obvious. The entrance pressure recovery coefficient on the continuous and discontinuous walls differs sharply. The discontinuous wall pressure recovery coefficient is extremely high compared to the continuous wall. Downstream the values of pressure coefficient merge quickly. As the spill flow ratio increases, the disparity between the initial points decreases. Again the pressure recovery coefficient increases to a certain level and tends to remain there as it did in the $^{s}/_{w} = 0$ case. The pattern is continued in the higher spill flow ratios (Figure 22): entrance pressure recovery coefficient disparity decreases with increasing $^{Q_s}/_{Q_i}$. For the highest spill flow ratios, the discontinuous wall curve dips below the continuous wall curve at $^{x}/_{w} = 4$. This apparently is caused by the severe streamline curvature near the discontinuous wall. For both $^{s}/_{w} = 0$ and $^{s}/_{w} = 1$, the disrupting effect on the flow pattern caused by the spill port are almost completely damped out at the end of the long receiver (L = 30W).

For the shorter wall, the effects are comparable to those of the longer wall. Figure 23 shows the shortest wall at $^{s}/_{w} = 0$. The flow is again accelerated as it was in the long wall case; however, the acceleration is not as large as before. The pressure recovery coefficient again rises with increasing spill flow. The next figure (24)

shows the peak in the recovery at $Q_s/Q_i = 0.5$ with the higher spill flow ratios showing a decline in the pressure recovery coefficient. After the switching of the jet, as indicated by the pressure recovery peak, the curves change from a convex shape to a concave shape. Figure 25 indicates two different states for the blocked load condition ($Q_s/Q_i = 1.0$). The flow pattern oscillates between these two different states at a low frequency. The next four graphs show the continuous and discontinuous walls plotted independently for clarity. The effects of the larger set-back are clearly visible (Figure 26). There is no acceleration of the fluid in the receiver. The pressure recovery coefficient increases until the jet switches and then decreases. Figure 27 shows the same switching effect as was seen for the long wall, $s/w = 1$. Figures 28 and 29 show the higher spill flow ratios. For these higher ratios, the pressure recovery coefficient drops slowly with increases in x/w, so that the last six spill flow ratios from $Q_s/Q_i = 0.5$ to 1.0 form a relatively narrow band of values.

Total pressure traverses between the two parallel walls are shown in Figures 30 through 37. The total pressure coefficient is plotted versus $Z/\frac{H}{2}$. The total pressure coefficient is given by $\frac{P_T - P_{20}}{1/2\rho\bar{V}_{t2}}$, where P_{20} is the static pressure at the end of the channel. This static pressure was chosen because at high spill flow ratios, the

static pressure in the channel occupied the major share of the total pressure, thereby making determination of the three-dimensionality of the velocity field difficult. The full traverses were found to be essentially symmetric, so only half of each traverse was plotted. For an aspect ratio of 8, the flow through the channel should be essentially two-dimensional at the midplane for low Q_s/Q_i. Figure 30 shows that the flow is essentially uniform in the Z direction, except for the end wall boundary layers, for Q_s/Q_i = 0.0. All of the curves are seen to be very flat except in the regions of the boundary layers on the opposite parallel side walls. For the lower Y/W values (traverses taken near the continuous wall), the distributions tend to have a thinner boundary layer than those traverses taken at the discontinuous wall. The magnitude of the centerplane total pressure coefficient is seen to rise with Y/W values from the continuous wall to 0.370. After the rise, the magnitude slowly starts to drop, reaching $\mathbb{P}$= 0.95 at Y/W=0.580. This rise and drop in the magnitude is due to the receiver channel wall boundary layers. For the higher spill flow ratio of Q_s/Q_i = 0.4 (Figure 31), the trend is essentially the same. That is, the total pressure coefficient rises to its maximum value then levels out. For the longer wall, the jet switches at Q_s/Q_i = 0.6. Figure 32 shows the effect of the switching on the two-dimensionality of the flow.

$Y/_W$ values close to the continuous wall show signs of a local three-dimensionality. The curves no longer rise to a maximum value and remain there, but dip back down and then rise again. Even at 30W downstream of the spill port, the effects of the spill port can be seen. The length of the longer wall has attenuated most of the non-uniformity caused by the switching in the Y direction (see Figure 15, centerplane velocity profile), but the Z direction displays some non-uniformities. These non-uniformities are more pronounced in the $Q_s/_{Q_i}$ = 0.8 case (Figure 33). The curves are seen to peak close to the parallel side plates and then decline to the midplane value. The peak indicates a region of high streamwise vorticity is produced as a result of the spill port being located near the parallel side walls. The presence of the streamwise vorticity is noticeable even for a low spill flow ratio ($Q_s/_{Q_i}$ = 0.1) for the short wall (Figure 34). Although the majority of the channel flow field is two-dimensional near the channel walls, some three-dimensionality exists. With the shorter walls, the attenuation of the non-uniformity that was seen earlier in the long wall receiver is no longer present. The effect of the spill port is noticeable for a significant distance downstream. Figure 35 shows a spill flow ratio of $Q_s/_{Q_i}$=0.4. The non-uniformity has increased and spread throughout most of the channel. The non-uniformity is less severe near

the discontinuous wall. Figure 36 shows that for $^{Qs}/_{Qi}$=0.6, the non-uniformity has already become quite severe with large dips in total pressure coefficient. For $^{Qs}/_{Qi}$ = 0.8 (Figure 37), the non-uniformity is extreme.

Figures 38 and 39 show lines of constant total pressure. The switching effect takes place between $^{Qs}/_{Qi}$=0.4 and $^{Qs}/_{Qi}$ = 0.5 for the shorter wall. In Figure 38 it can be seen that the non-uniformity is greater near the discontinuous wall after the jet switches. Three regions of high total pressure indicate the possible existence of streamwise vorticity in the form of a vortex located near each end wall at about a distance of 0.1 [$^{Z}/_{H/2}$] from each wall. The center of each high total pressure region is off midplane by $^{Y}/_{W}$ = 0.25. The dashed lines indicate the probable contours followed for which no data points could be obtained.

5. Conclusions

For a wall jet impinging on a receiver, two distinct states can be defined. In the first state, the wall jet remains attached to the continuous wall with an increase in the static pressure coefficient for increasing spill flow. In the second state, the wall jet has switched to the vented (discontinuous) wall, and the static pressure coefficient decreases with increases in spill flow. This switching takes place at lower spill flow ratios as the setback is increased. Most of the flow non-uniformity created by the spill port is smoothed out by the time it reaches the exit of the longest wall. For the shorter wall, the non-uniformities are quite noticeable at the receiver exit, even for the smaller spill flow ratios. The short wall also proves to be slightly unstable at the blocked load condition. The pressure coefficient for the blocked case shifts from one set of values to another with a low frequency periodicity.

Bibliography

(1) Hill, P. G., "Turbulent Jets in Ducted Streams", Journal of Fluid Mechanics, Vol. 22, No. 1, (1965), pp. 161-186

(2) Hill, P. G., "Incompressible Jet Mixing in Converging-Diverging Axisymmetric Ducts", Journal of Basic Engineering, Trans. ASME, Series D, Vol. 89, No. 1, (March, 1967), p. 210

(3) Hickman, K. E.; Hill, P. G.; Gilbert, G. B., "Analysis and Testing of Compressible Flow Ejectors with Variable Area Mixing Tubes", ASME Paper No. 72 FE-14

(4) Heskestad, G., "An Edge Suction Effect", AIAA Journal, Vol. 3 (1965), pp. 1958-1961

(5) Tillman, E. S., Jr., and Sisto, F., Jr., "Deflection and Diffusion of a Rectangular Jet by the Edge Suction Effect", Journal of Hydronautics, Vol. 1, No. 2, p. 108

(6) Heskestad, G., "A Suction Scheme Applied to Flow Through Sudden Enlargement", Journal of Basic Engineering, Trans. ASME, Series D, Vol. 90, p. 541

(7) Heskestad, G., "Further Experiments with Suction at a Sudden Enlargement in a Pipe", Journal of Basic Engineering, Trans. ASME, Series D, Vol. 92, p. 437

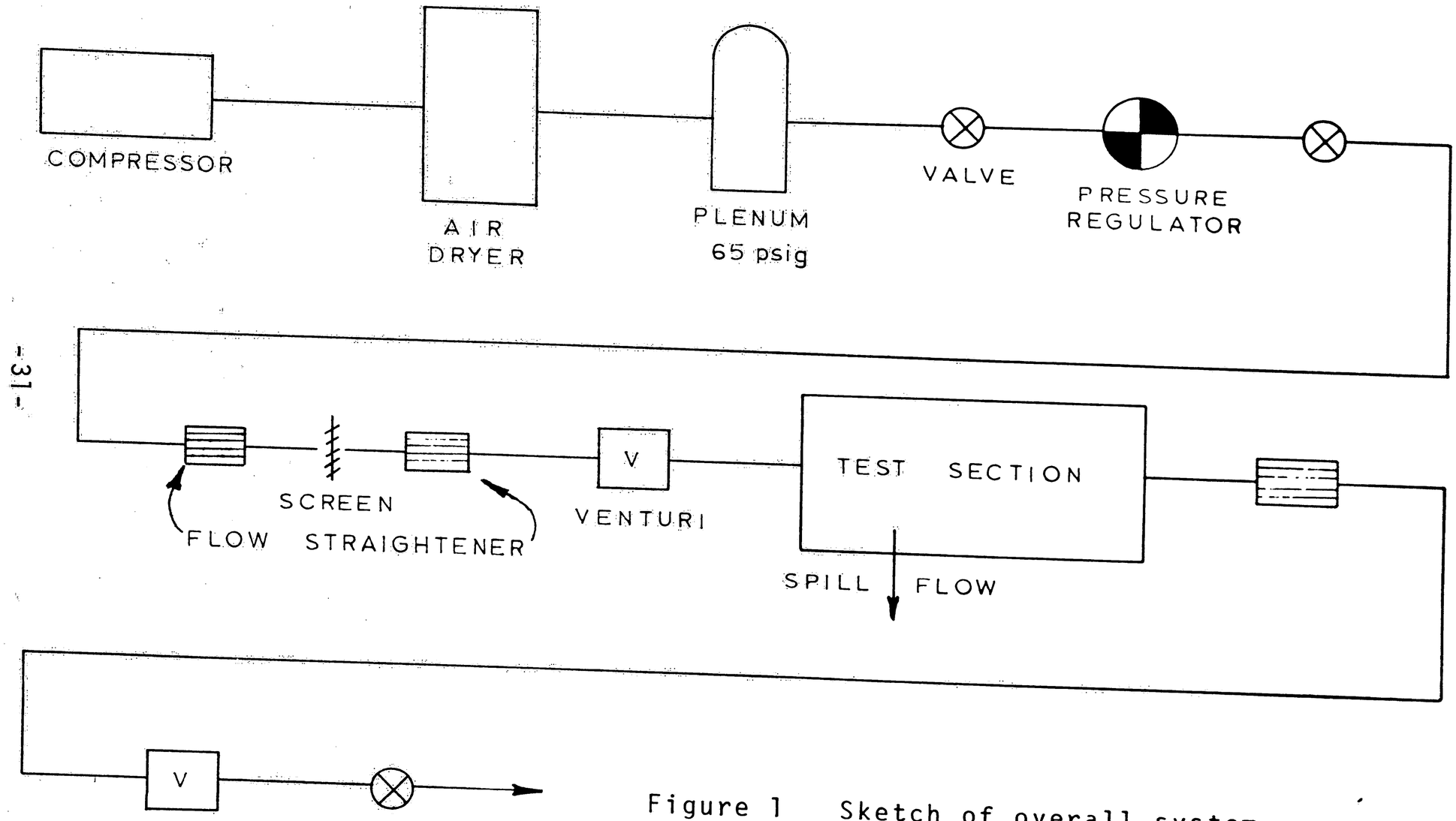

Figure 1 Sketch of overall system

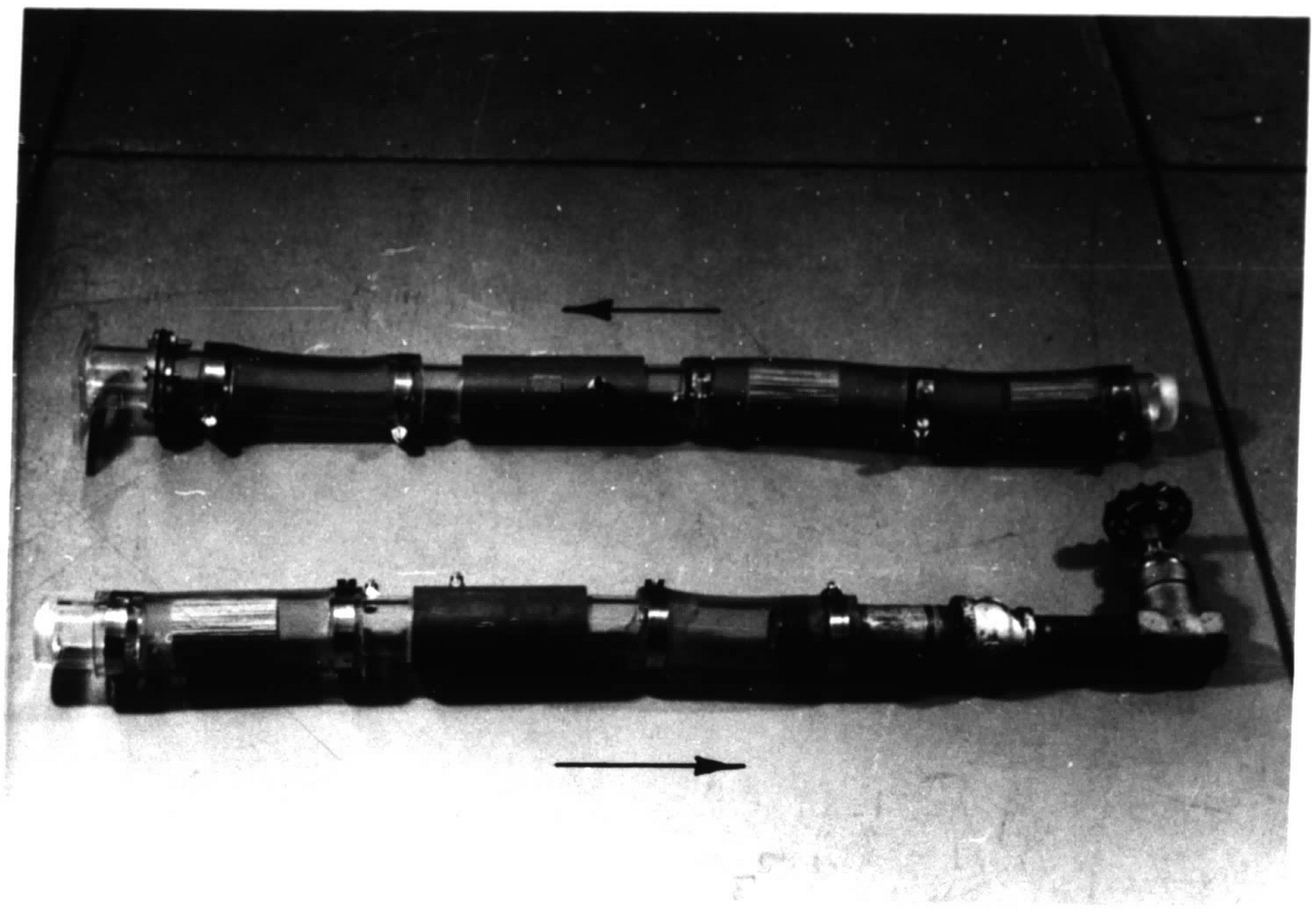

Figure 2 Flow systems upstream and downstream of the test section

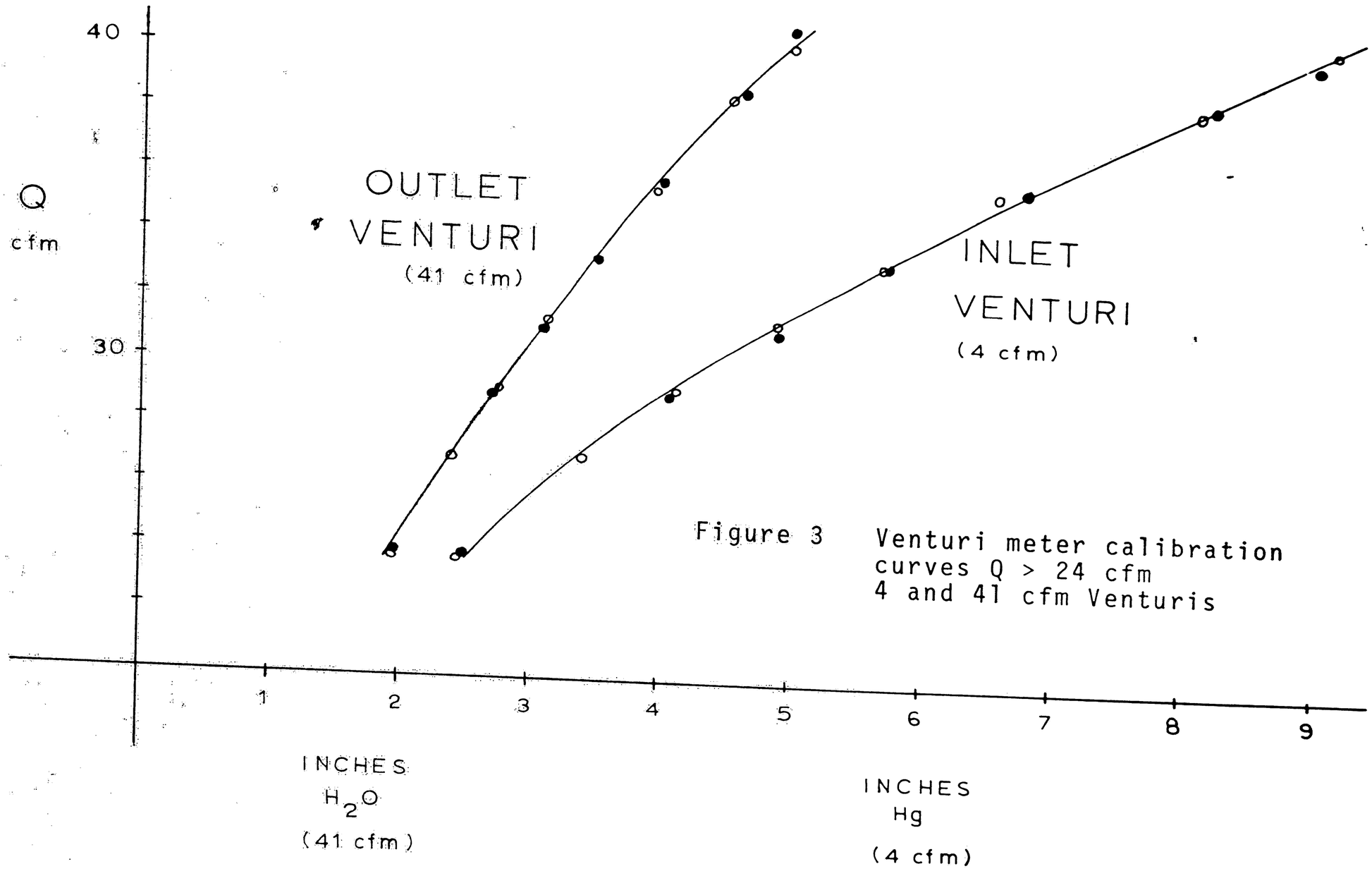

Figure 3 Venturi meter calibration curves Q > 24 cfm 4 and 41 cfm Venturis

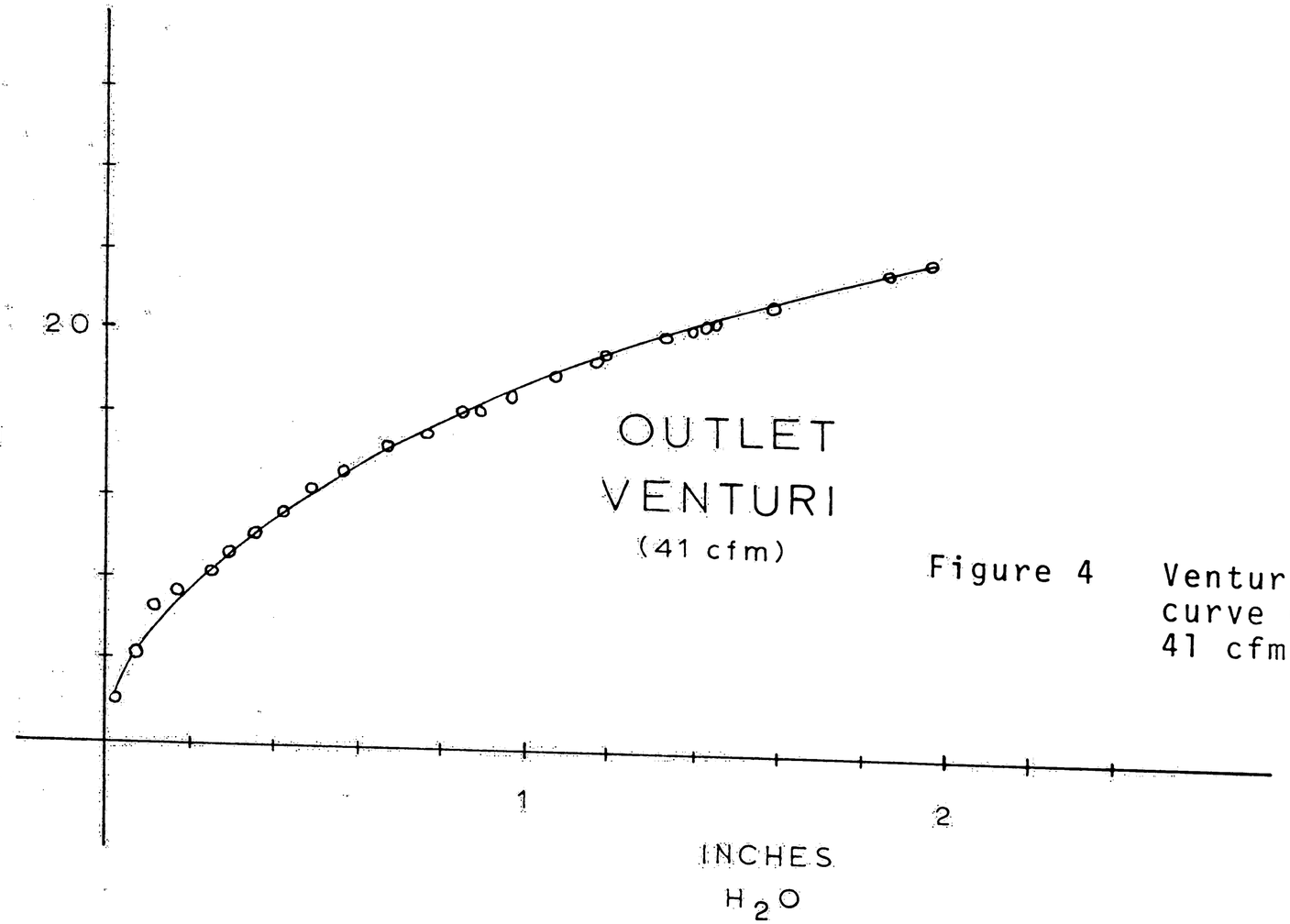

Figure 4 Venturi meter calibration curve Q < 24 cfm
41 cfm Venturi only

ALL DIMENSIONS IN INCHES

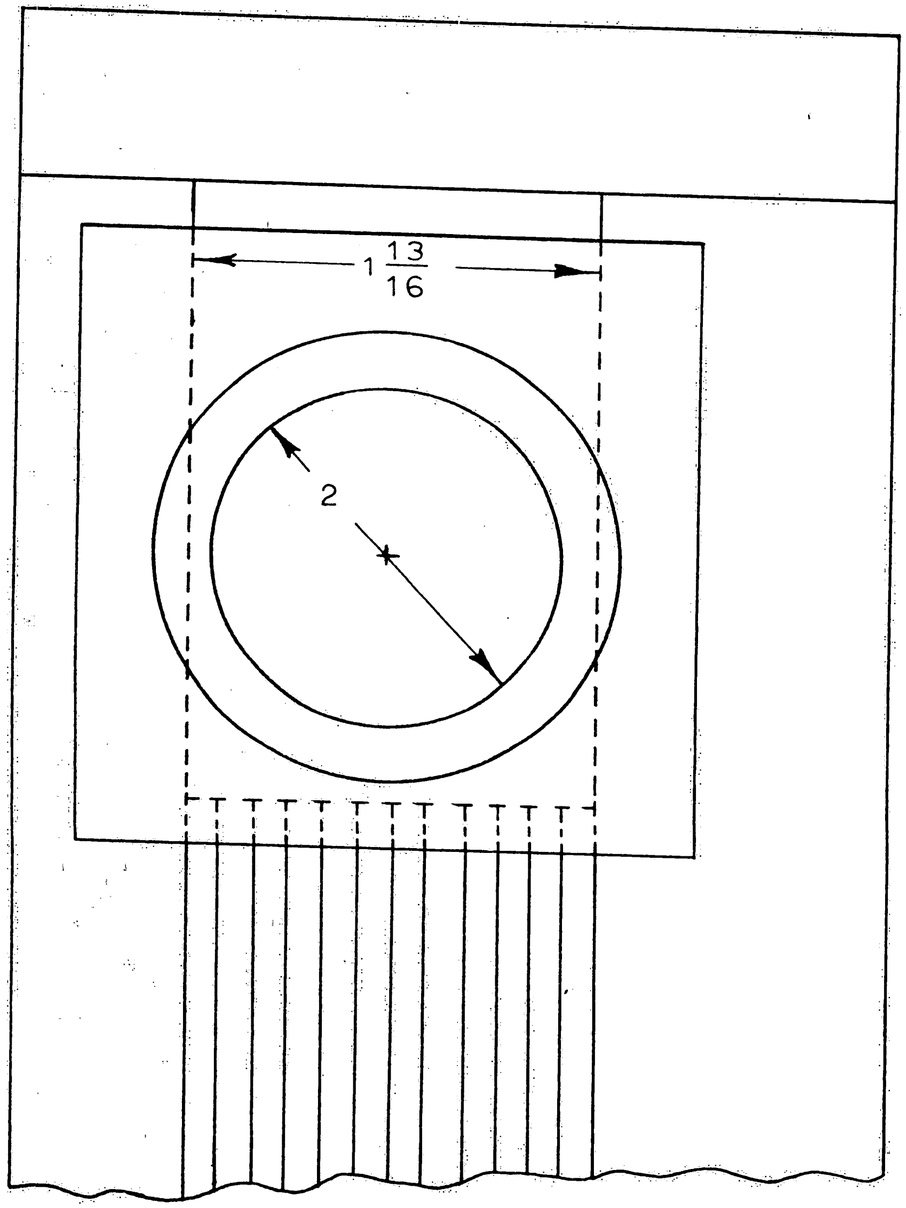

TOP VIEW

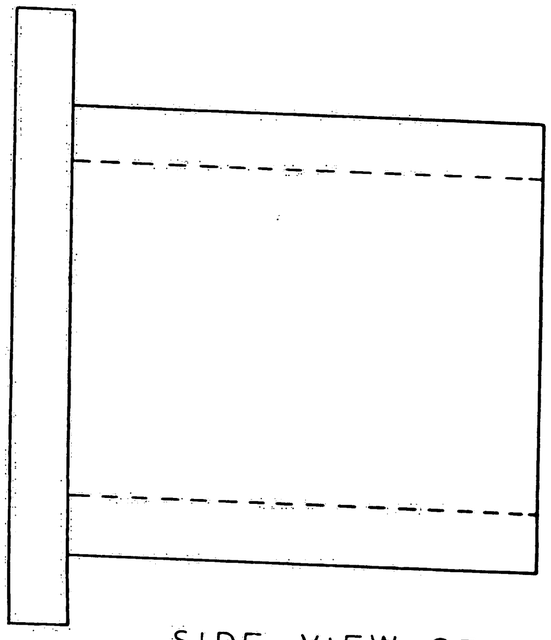

SIDE VIEW OF
PERPENDICULAR INLET

Figure 5 Sketch of perpendicular inlet

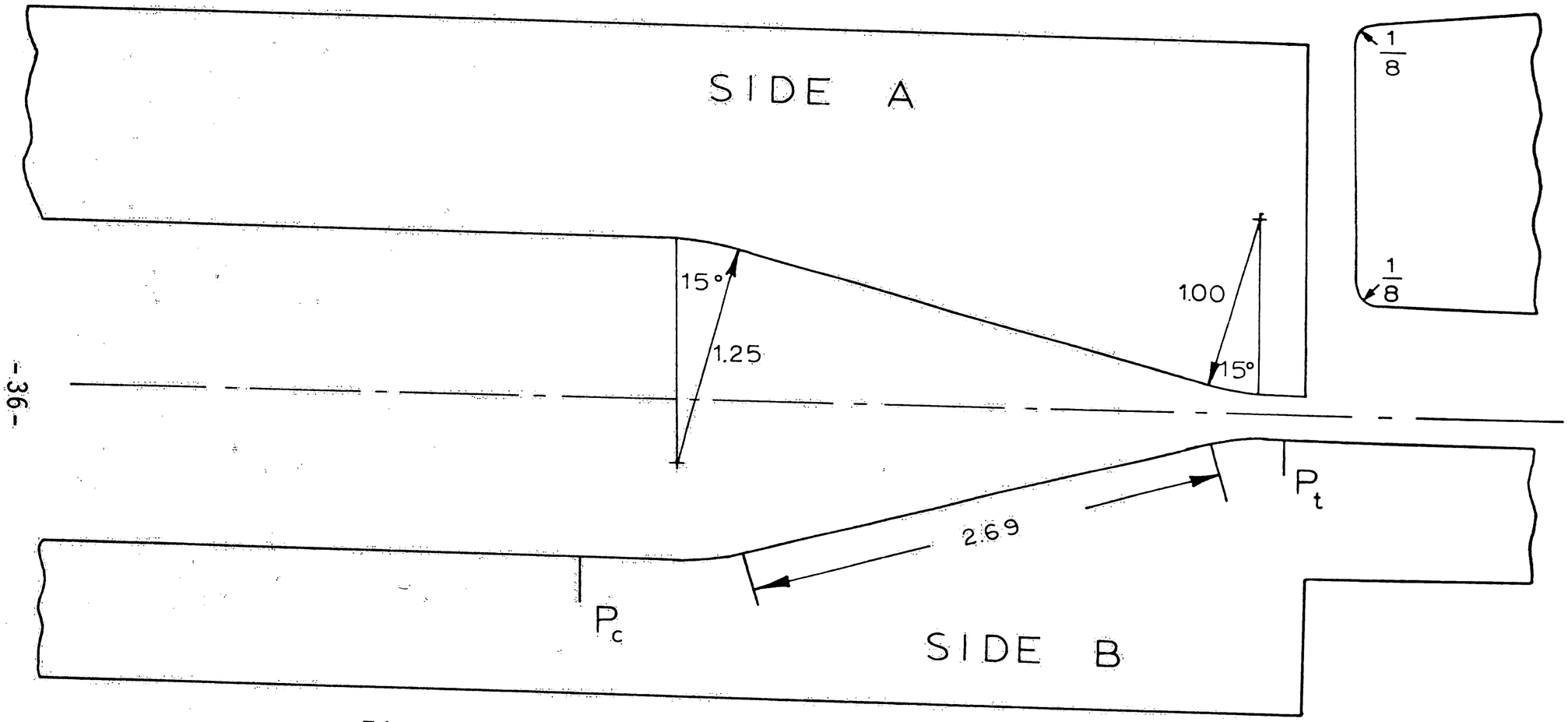

Figure 6 Sketch of nozzle dimensions

HALF SCALE

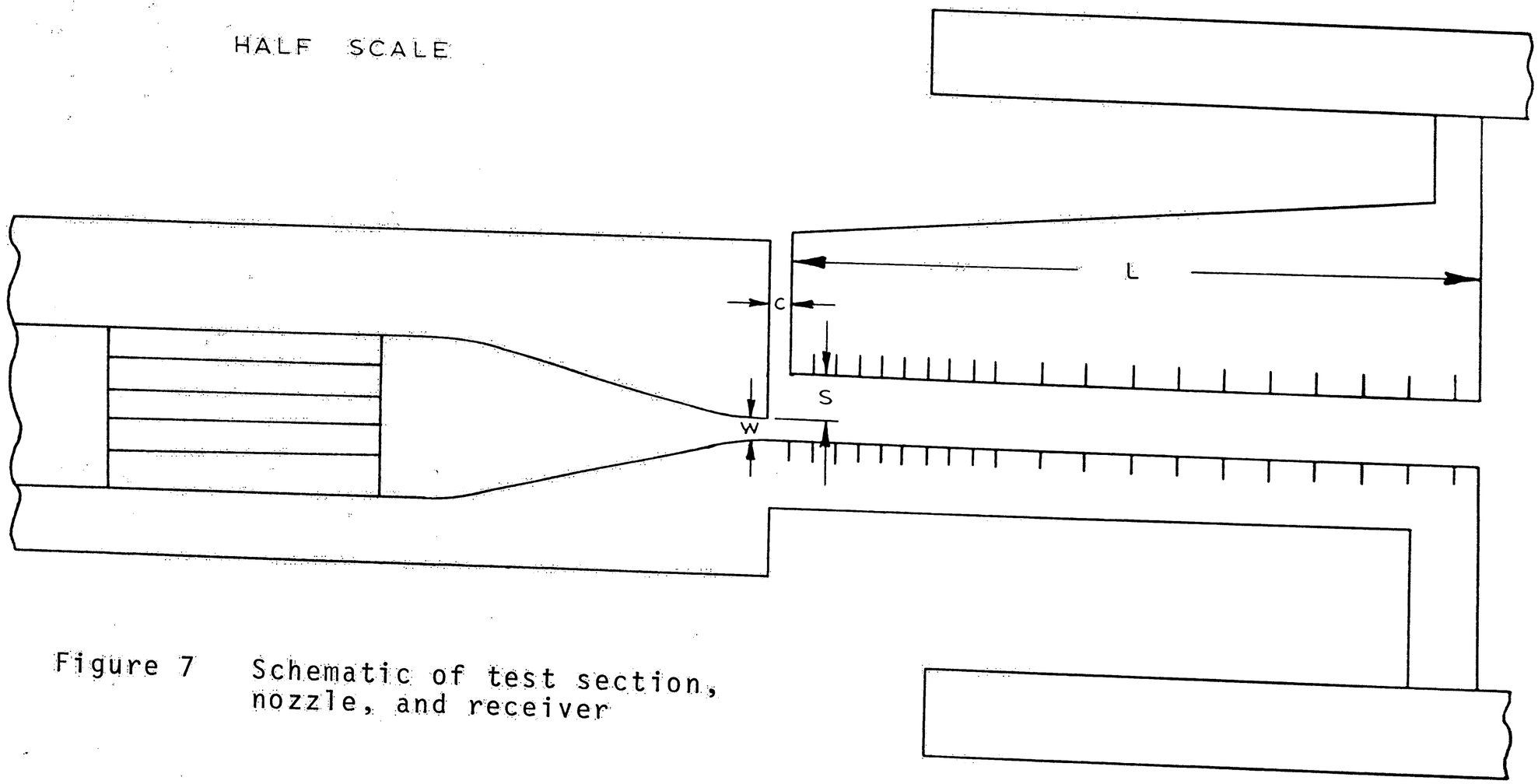

Figure 7 Schematic of test section, nozzle, and receiver

HALF SCALE

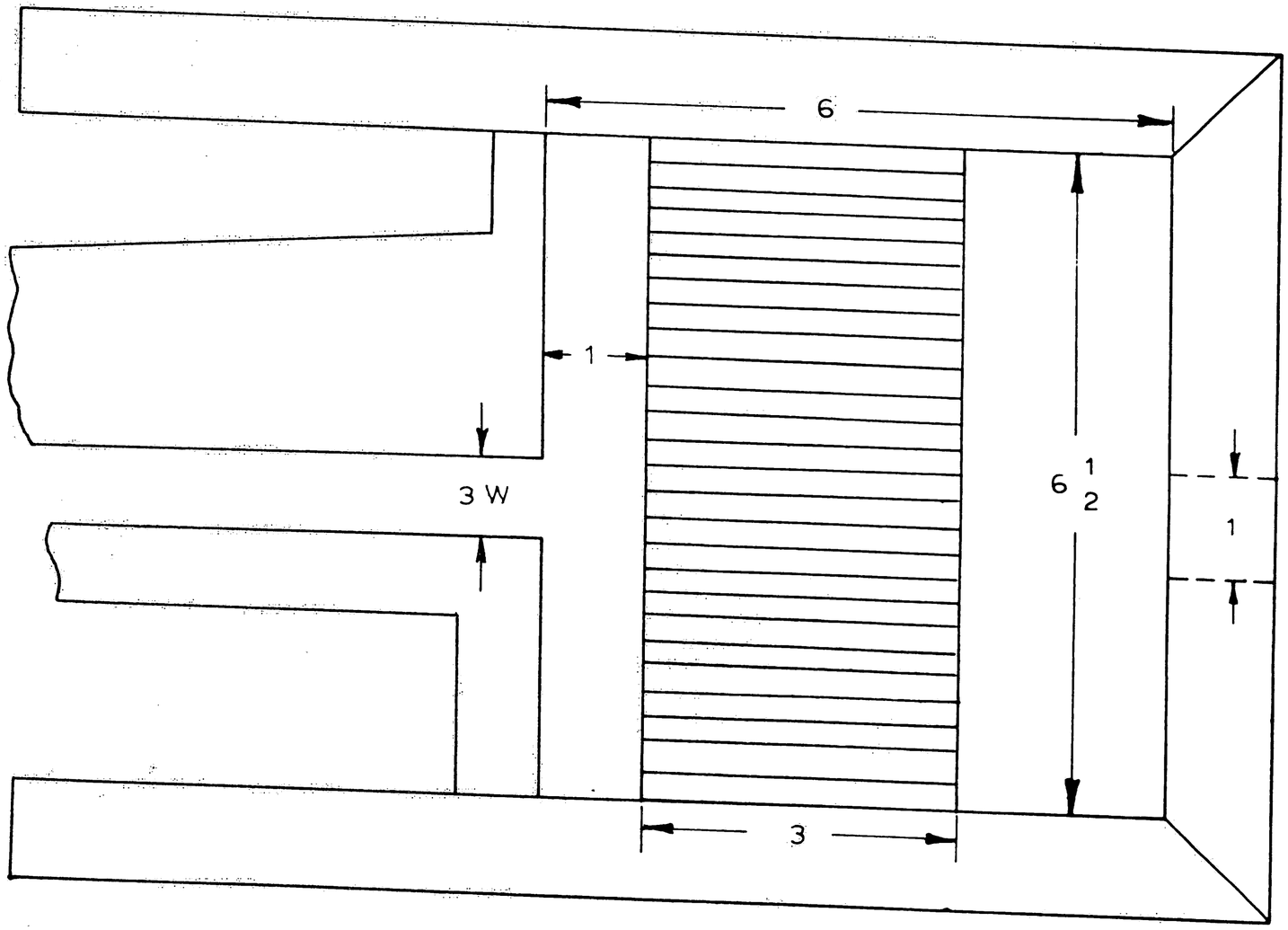

Figure 8 Sketch of plenum chamber

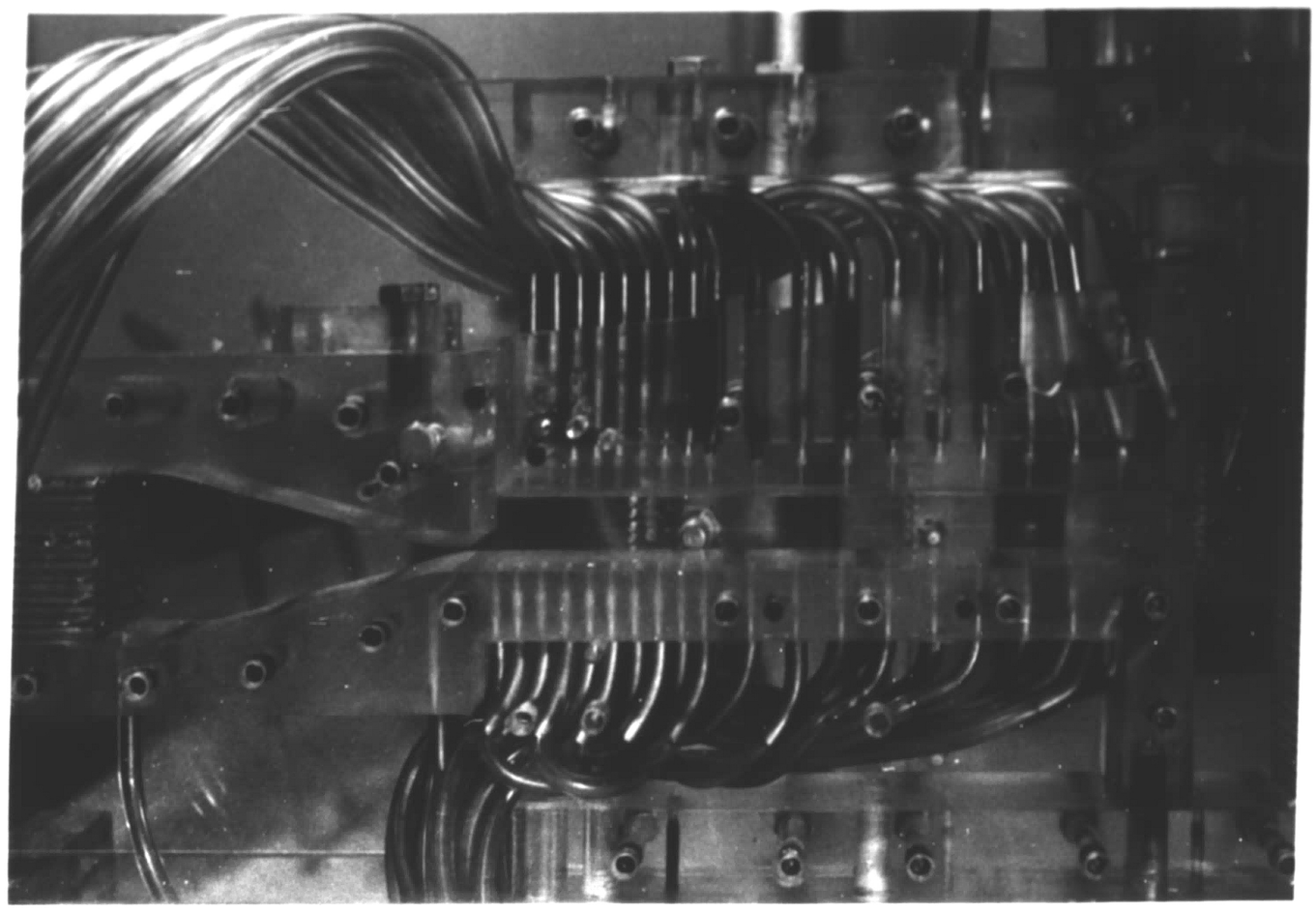

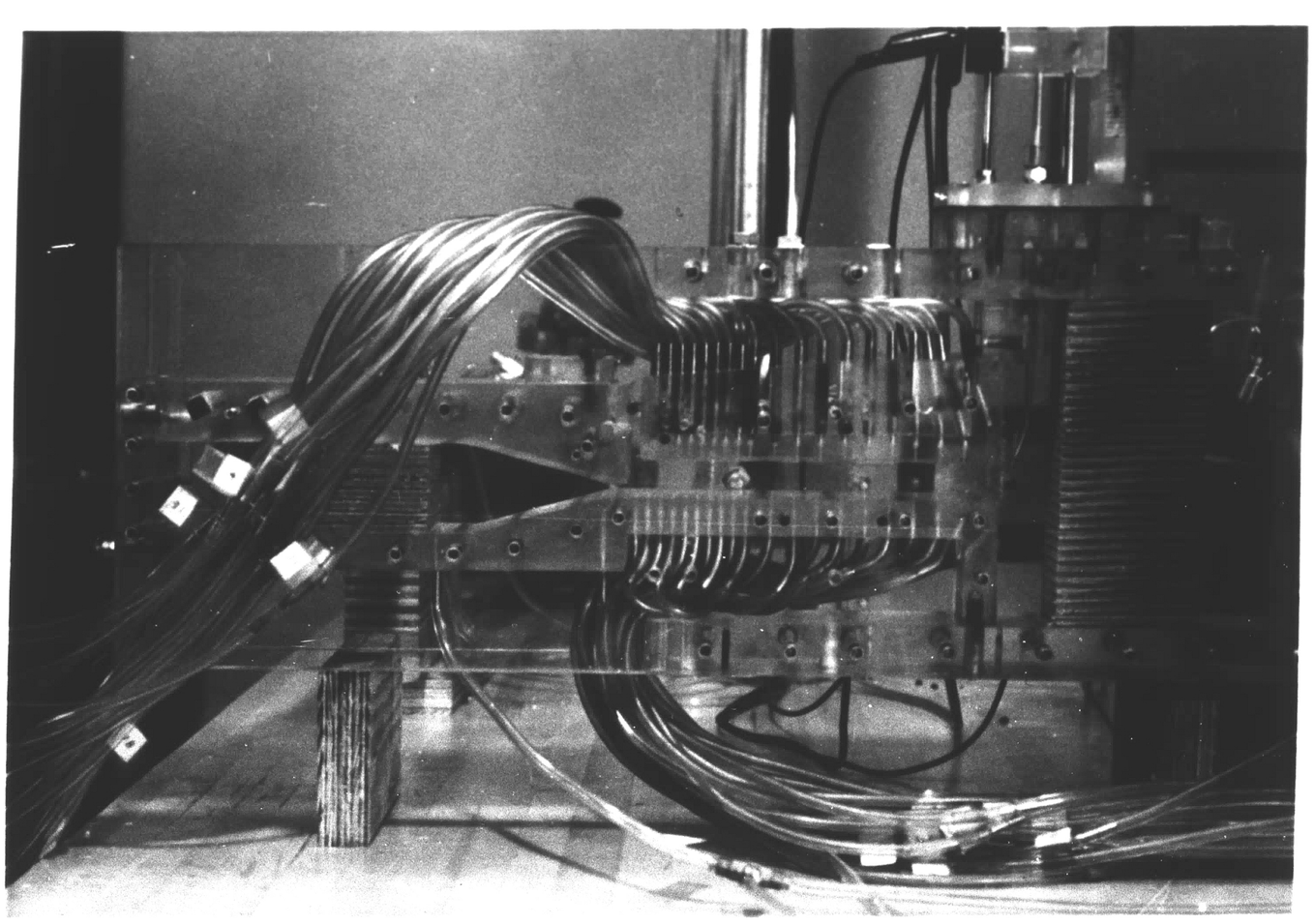

Figure 9 Pictures of experimental apparatus

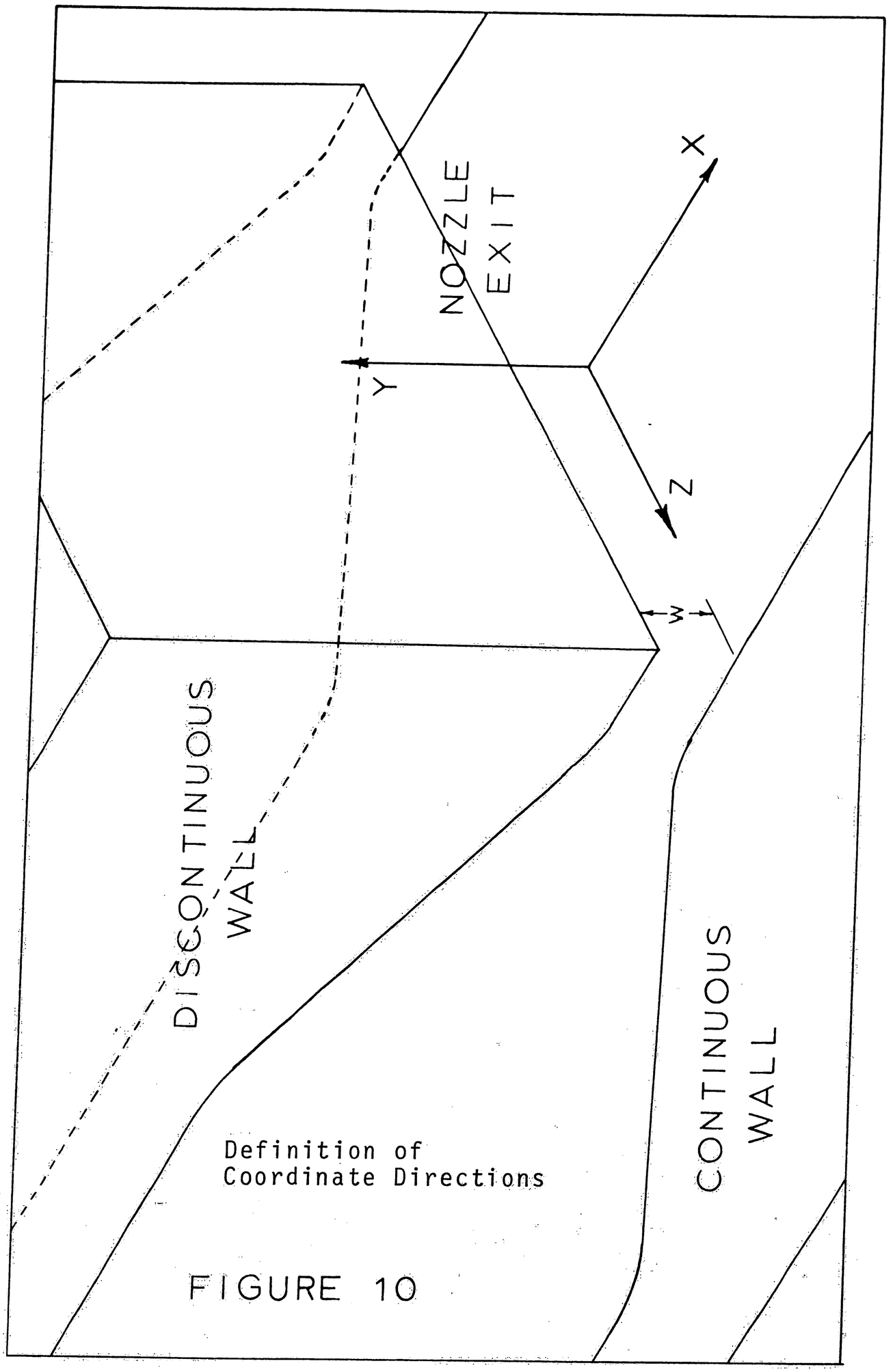
NOZZLE
EXIT
X
Y
Z
W
DISCONTINUOUS
WALL
CONTINUOUS
WALL
Definition of
Coordinate Directions

FIGURE 10

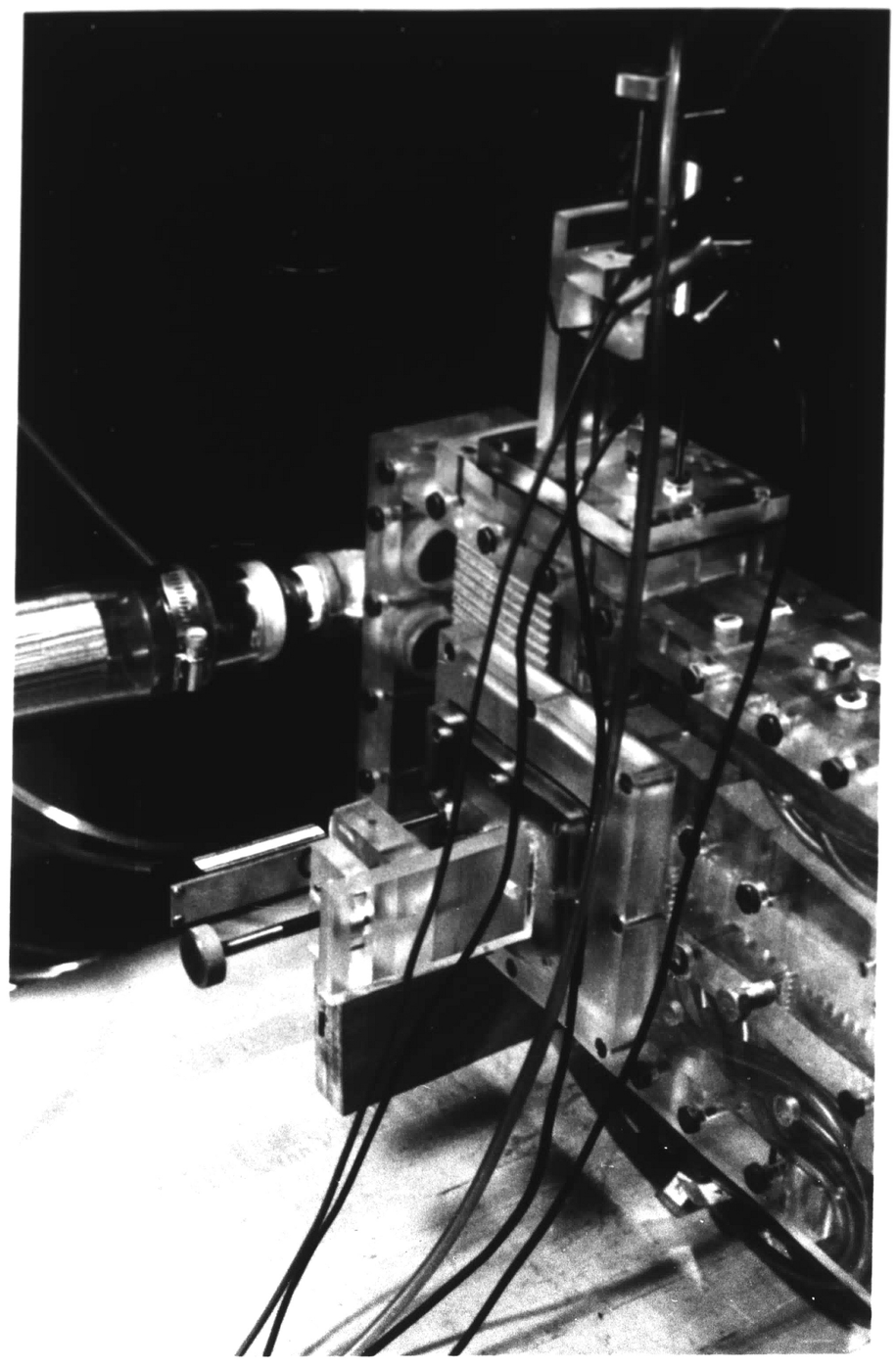

Figure 11 Traversing mechanism

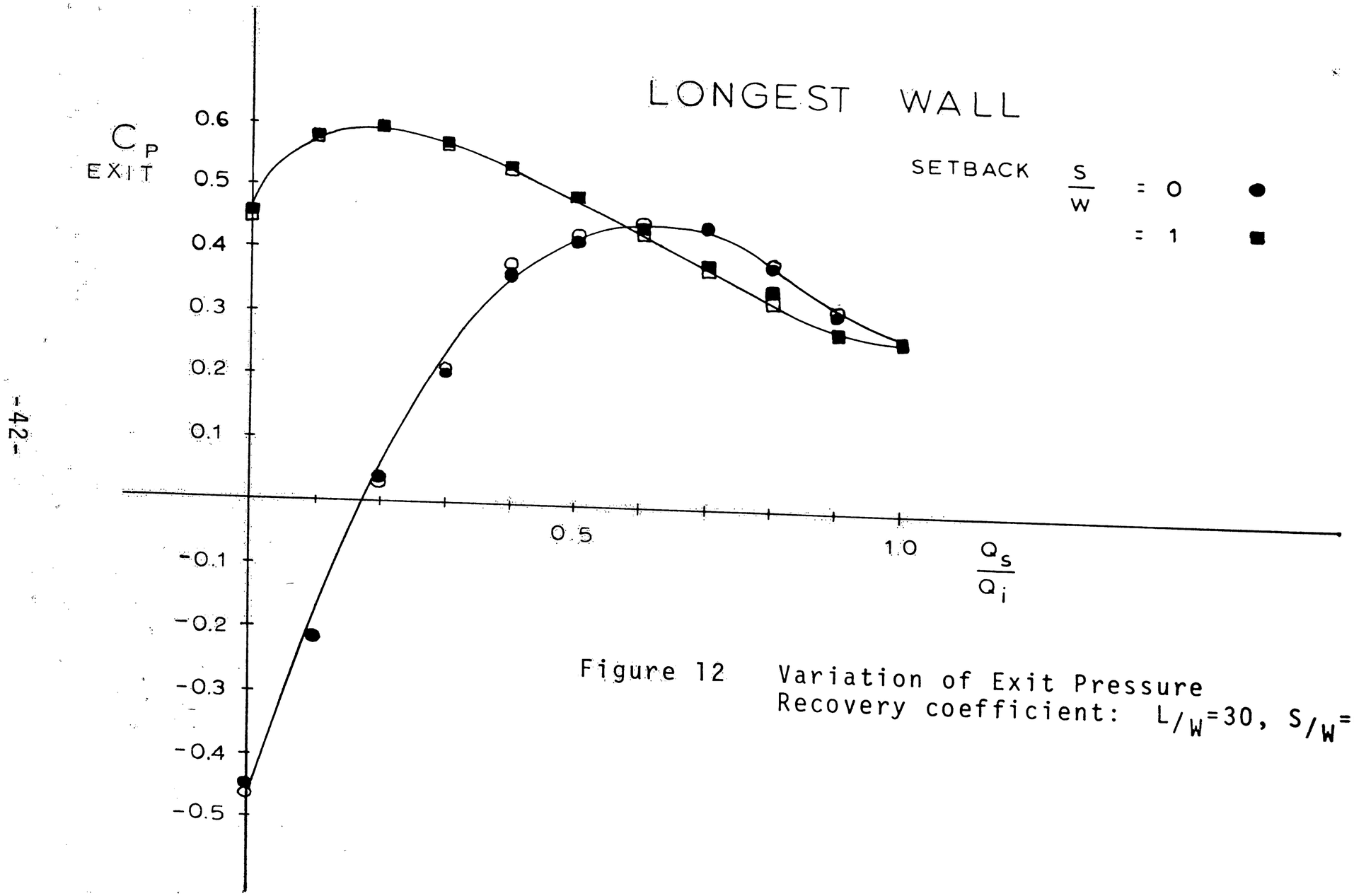

Figure 12 Variation of Exit Pressure Recovery coefficient: $L/W=30$, $S/W=0, 1$

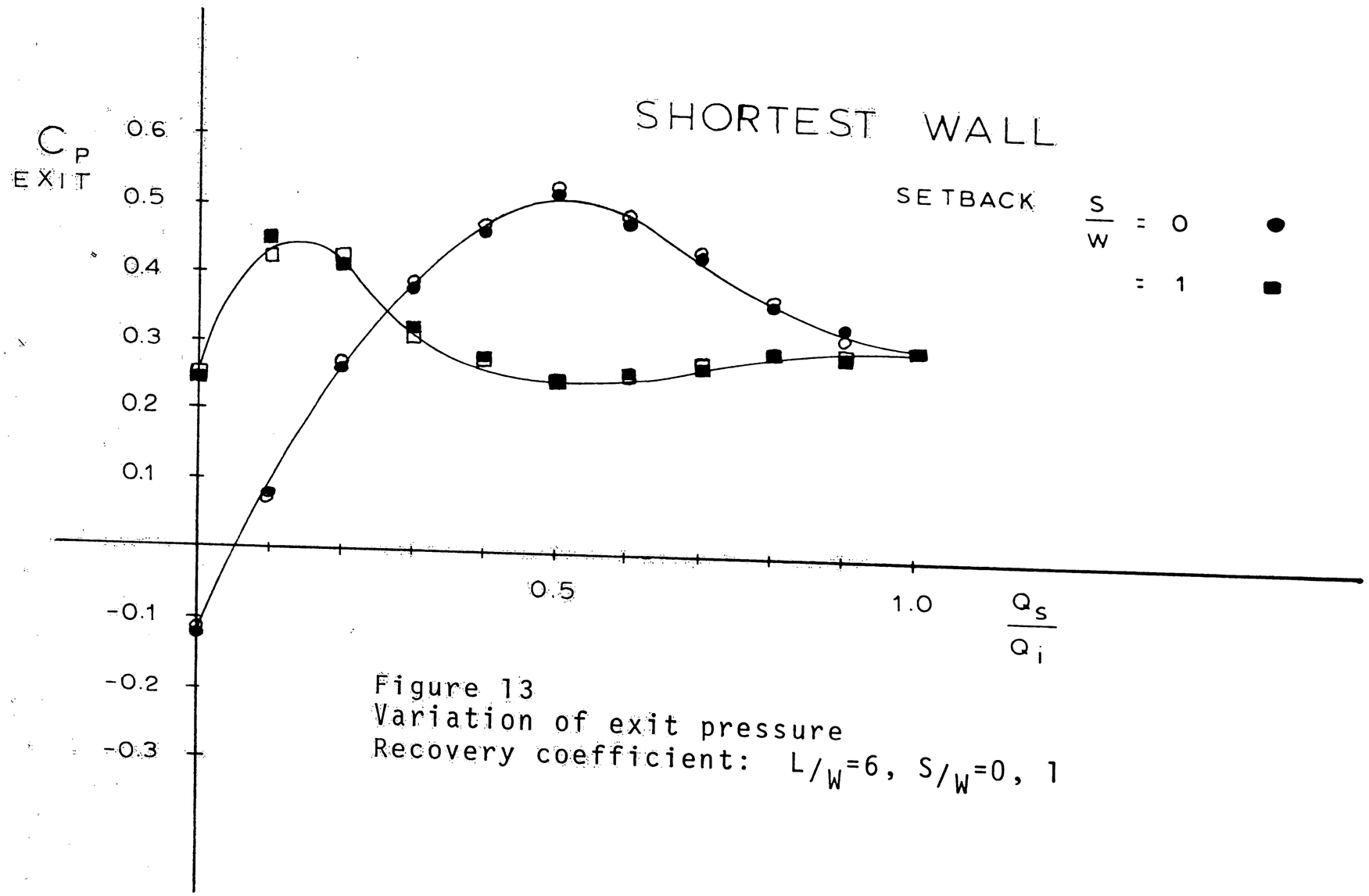

Figure 13
Variation of exit pressure
Recovery coefficient: $L/_W=6$, $S/_W=0$, 1

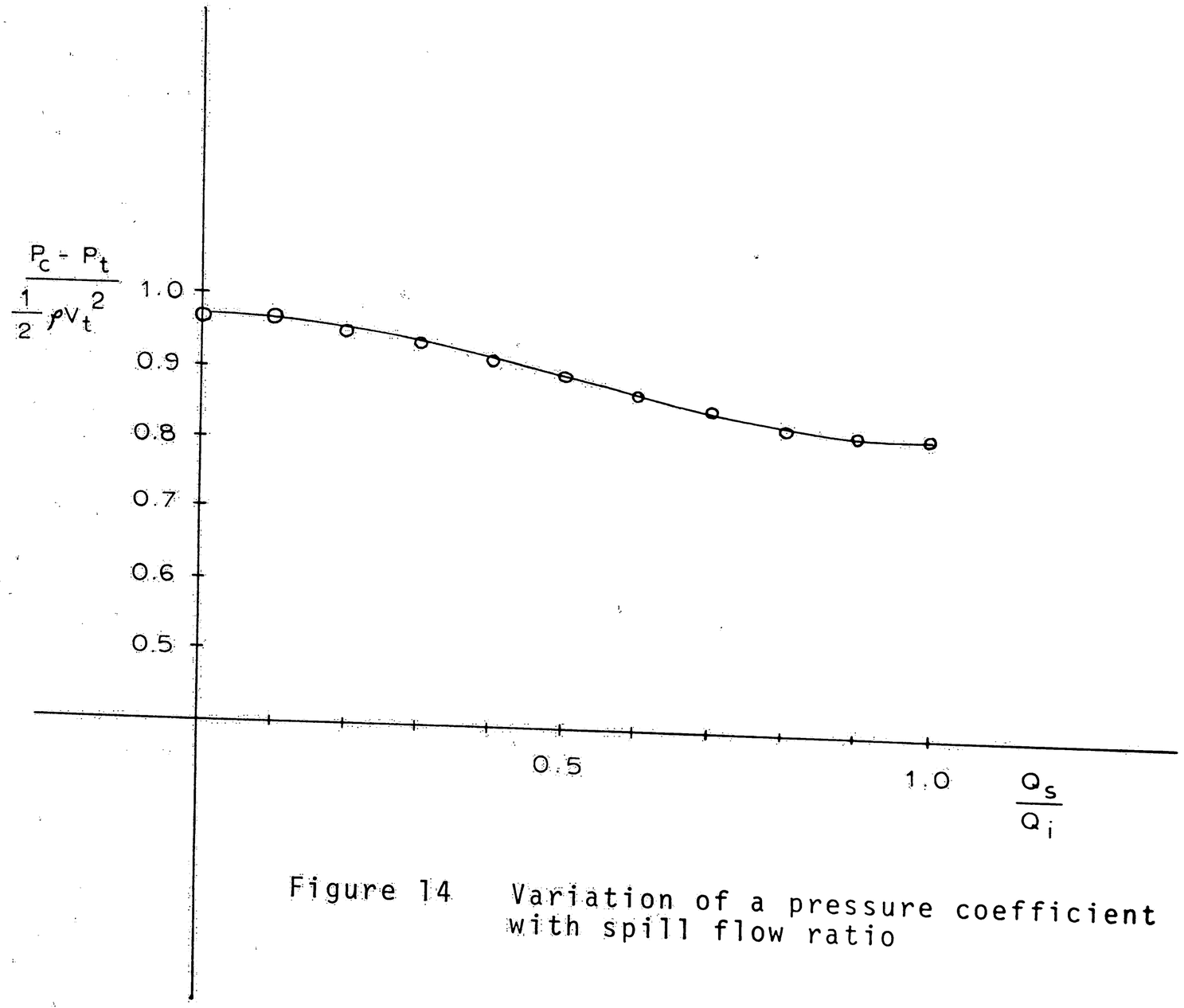

Figure 14 Variation of a pressure coefficient with spill flow ratio

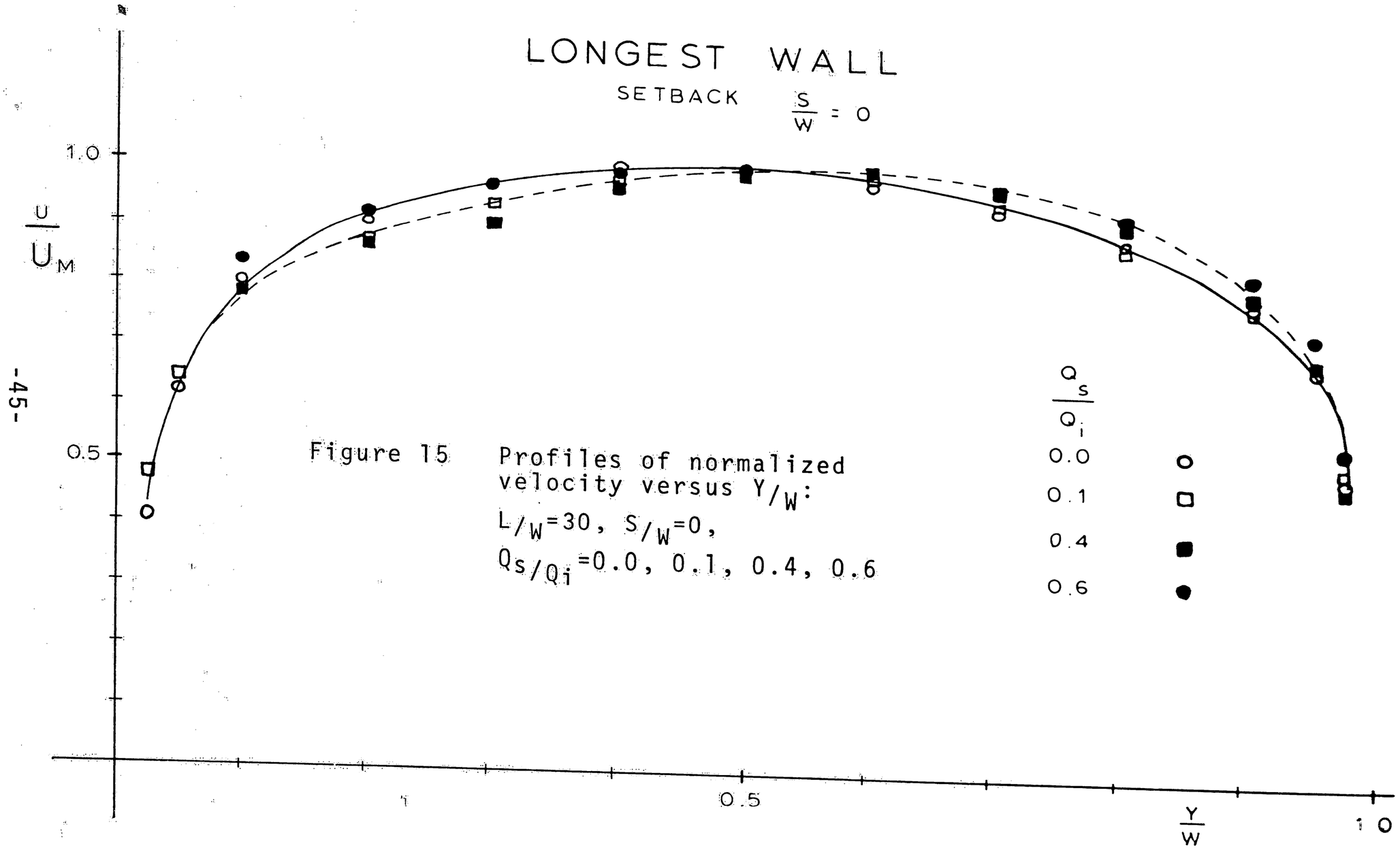

Figure 15 Profiles of normalized velocity versus Y/W:
$L/W=30$, $S/W=0$,
$Q_{s/Q_i}=0.0, 0.1, 0.4, 0.6$

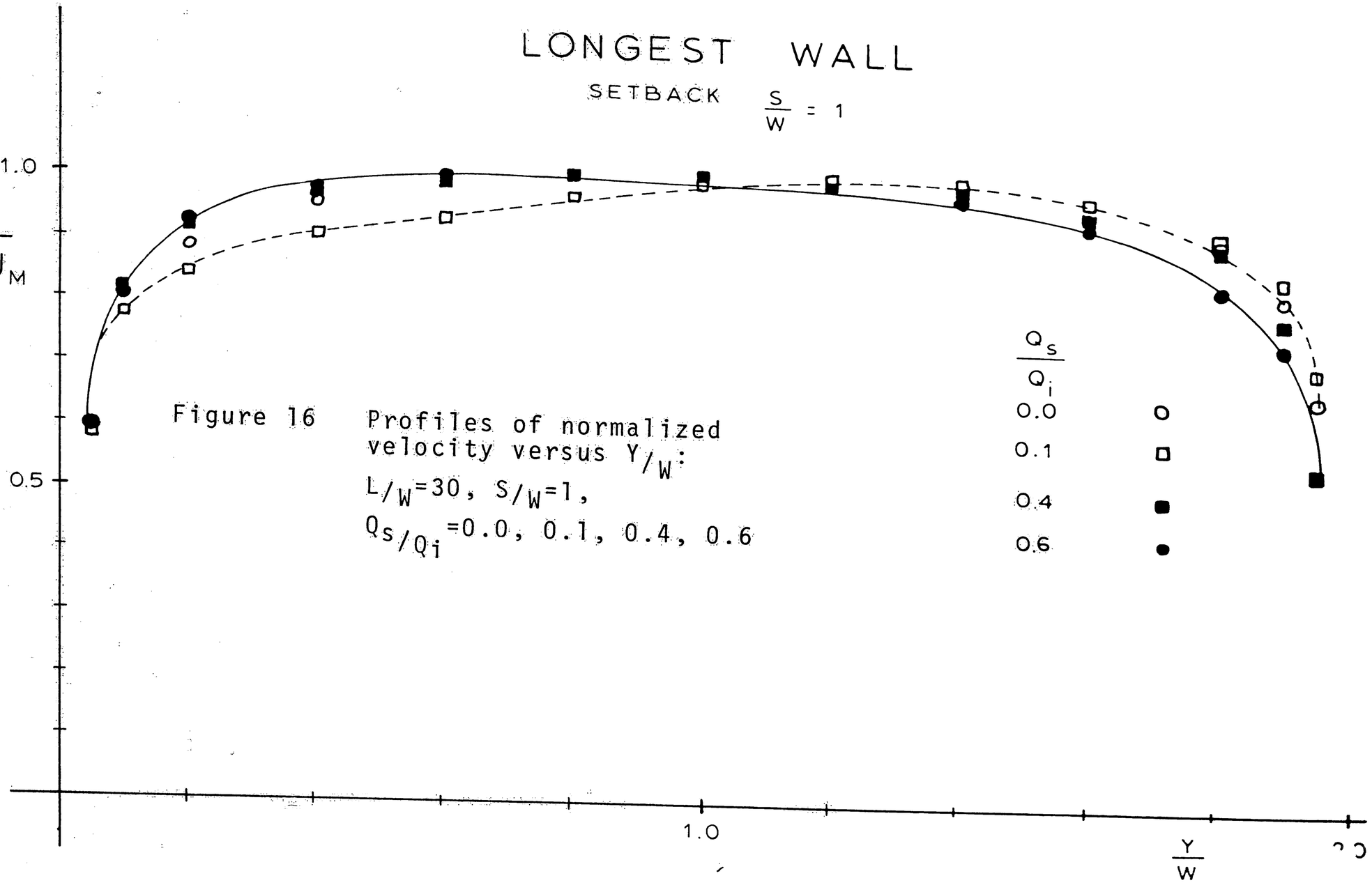

Figure 16 Profiles of normalized velocity versus Y/W:
$L/W=30$, $S/W=1$,
$Q_{s/Q_i}=0.0, 0.1, 0.4, 0.6$

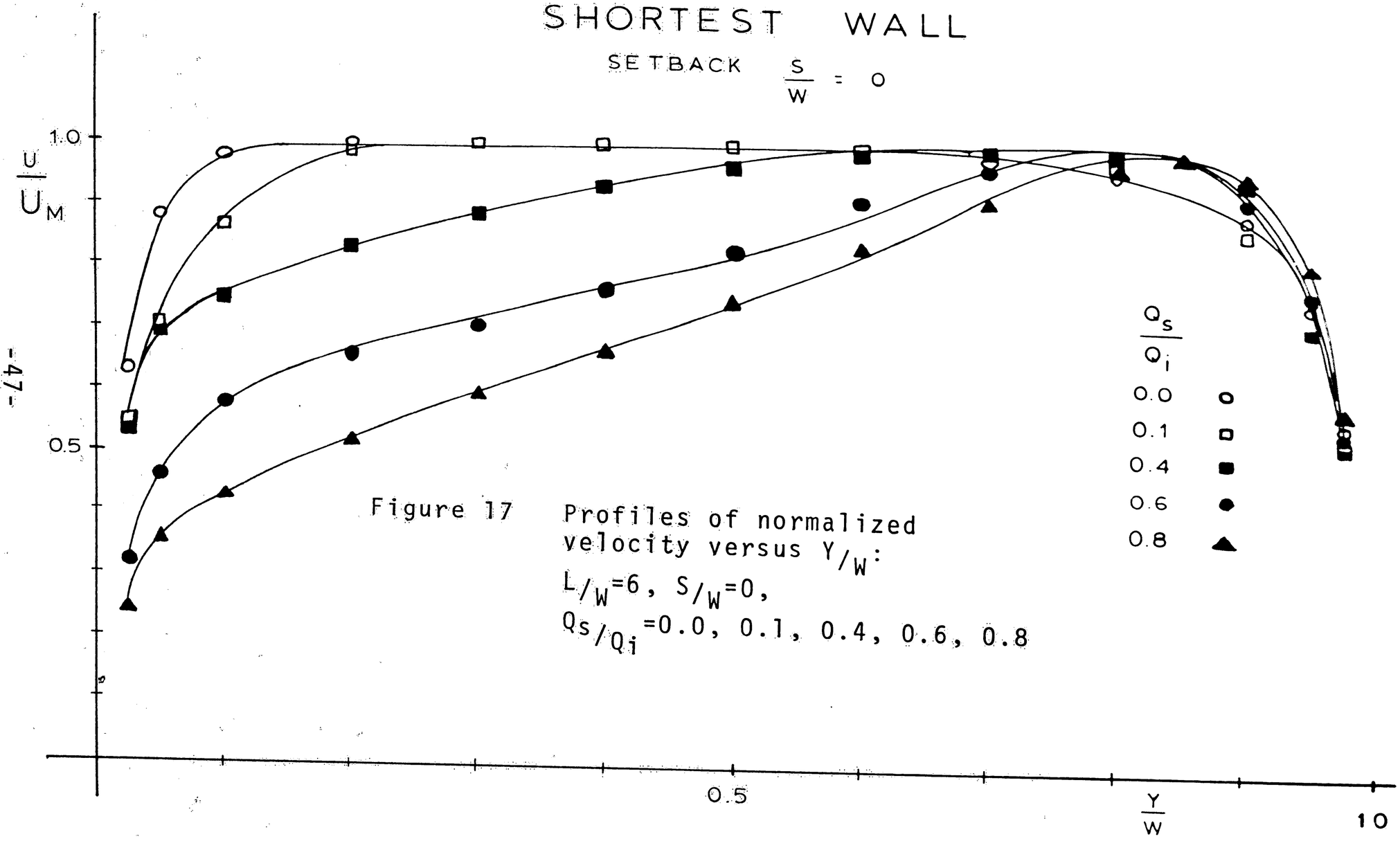

Figure 17 Profiles of normalized velocity versus Y/W: $L/W=6$, $S/W=0$, $Qs/Qi=0.0, 0.1, 0.4, 0.6, 0.8$

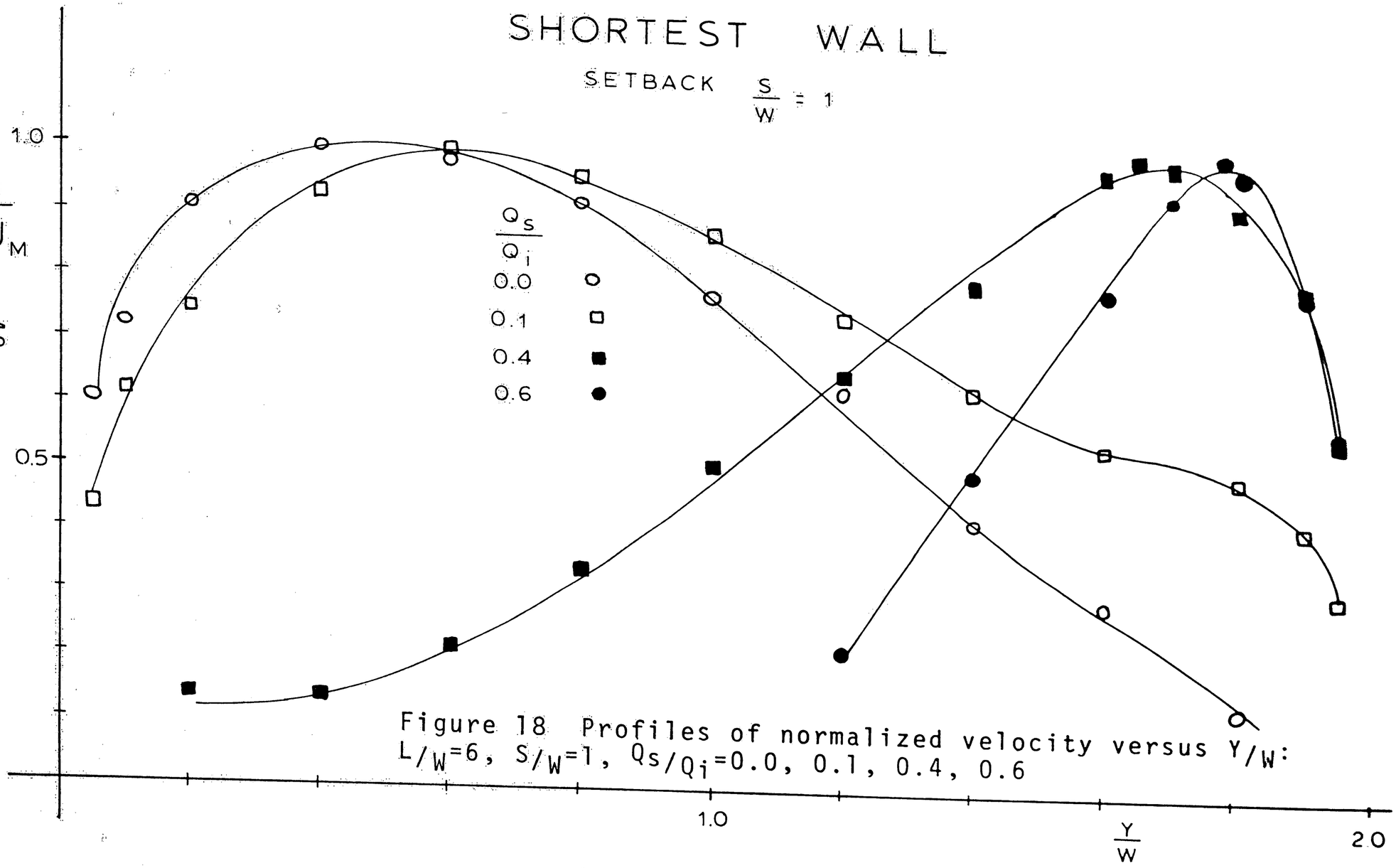

Figure 18 Profiles of normalized velocity versus Y/W: $L/W=6$, $S/W=1$, $Q_s/Q_i=0.0$, 0.1, 0.4, 0.6

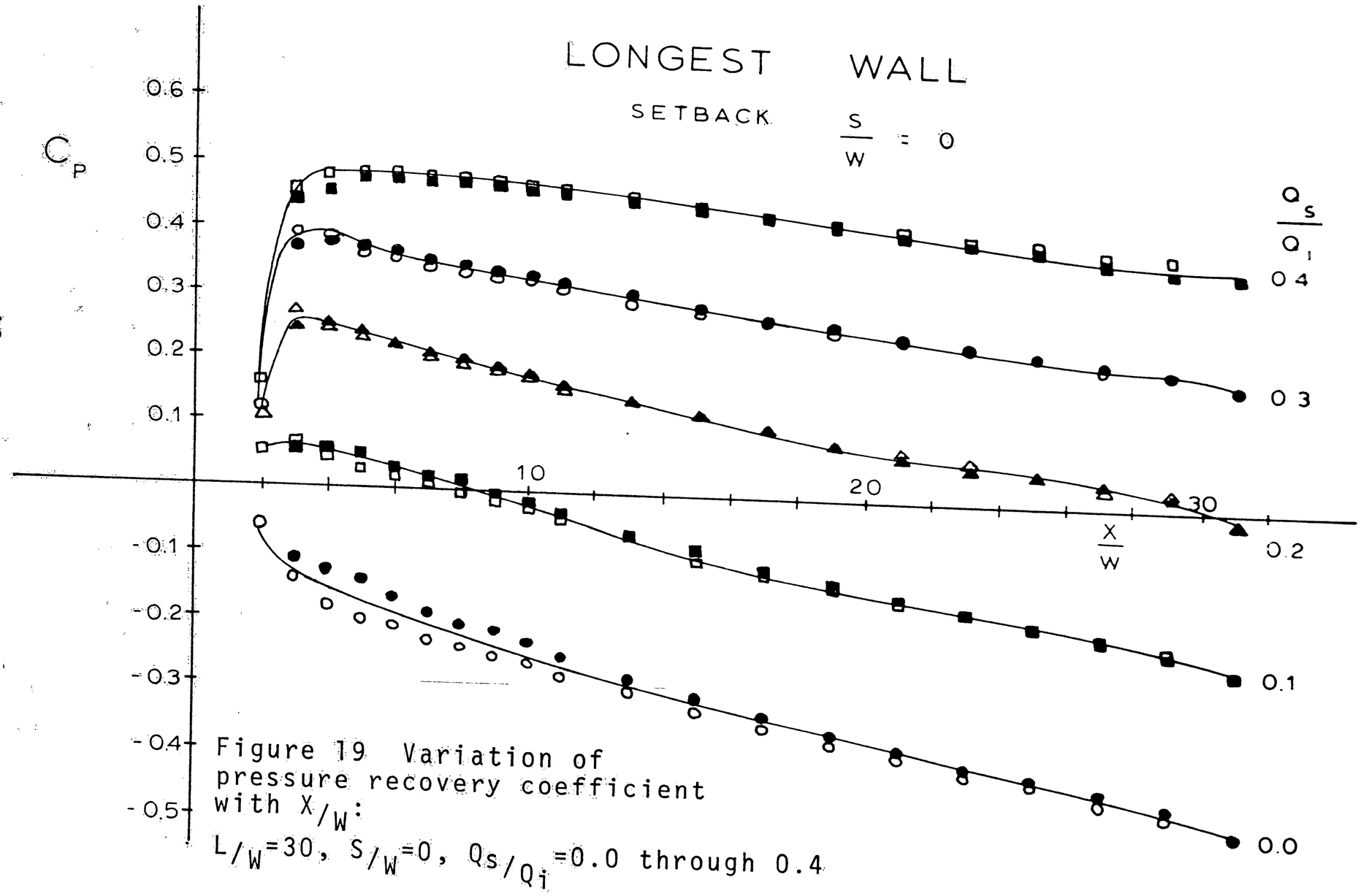

Figure 19 Variation of pressure recovery coefficient with X/W:
$L/W=30$, $S/W=0$, $Qs/Qi=0.0$ through 0.4

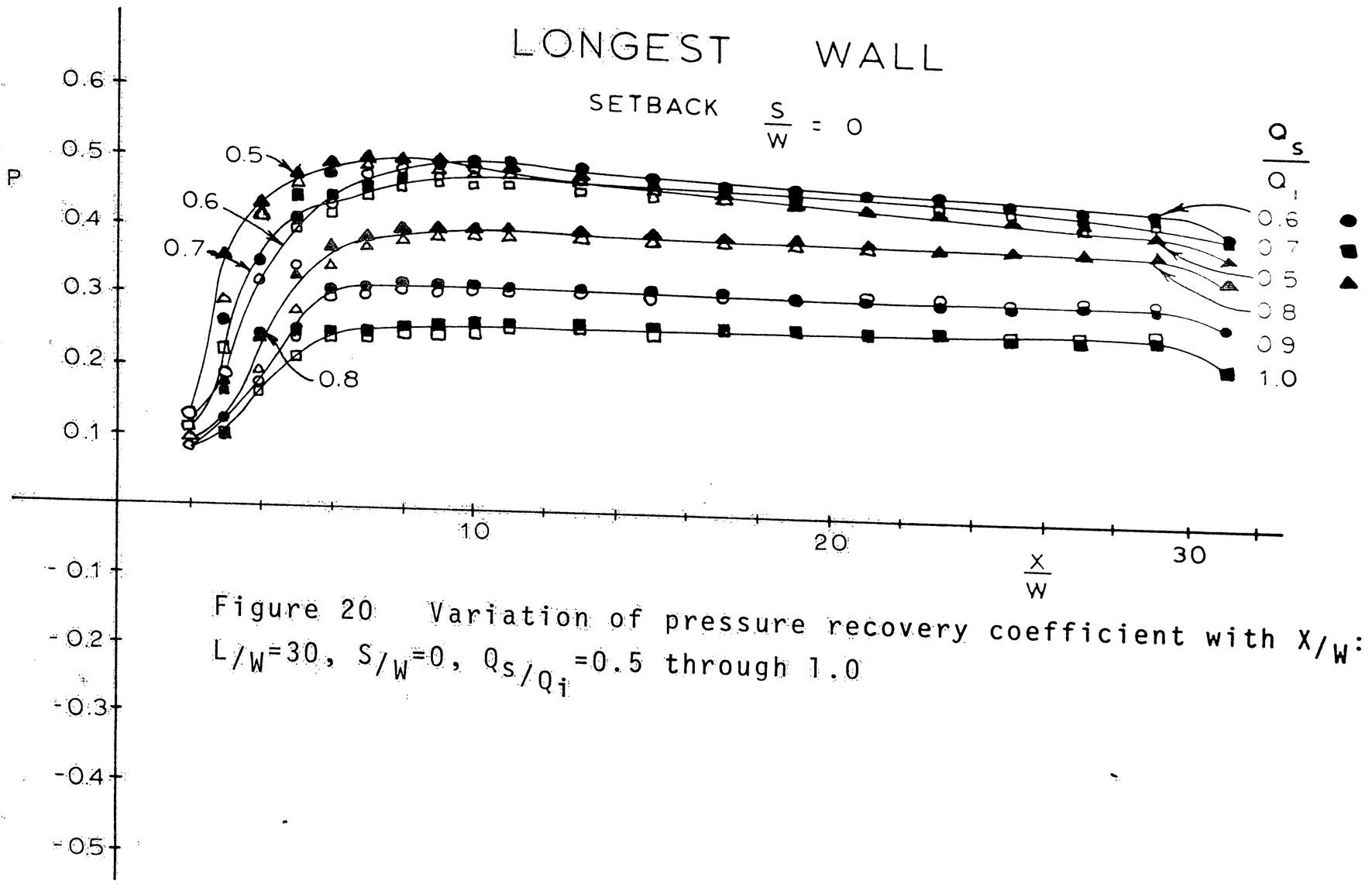

Figure 20 Variation of pressure recovery coefficient with X/W: $L/W=30$, $S/W=0$, $Q_{S/Q_i}=0.5$ through 1.0

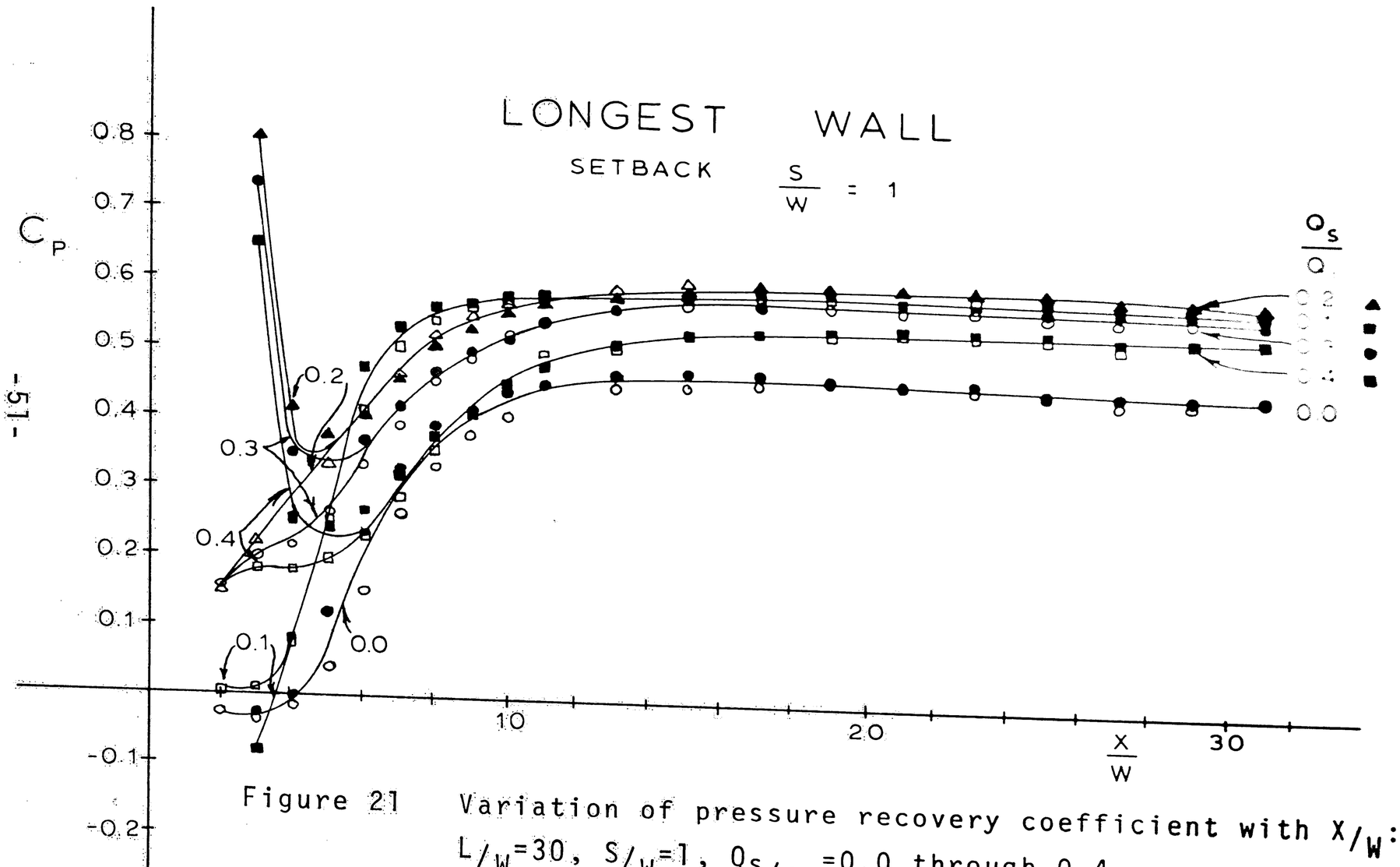

Figure 21 Variation of pressure recovery coefficient with X/W: $L/W=30$, $S/W=1$, $Qs/Qi=0.0$ through 0.4

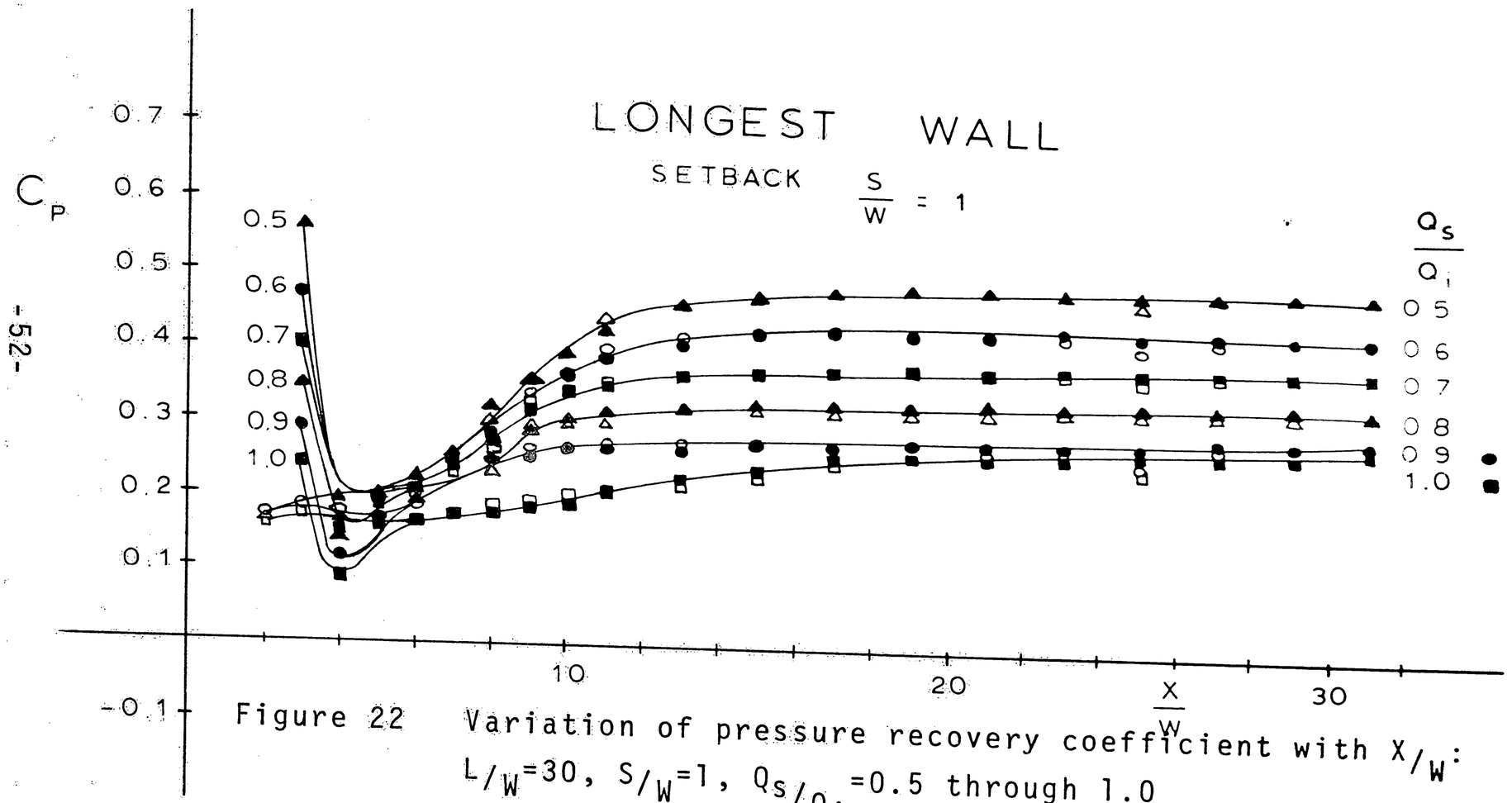

Figure 22 Variation of pressure recovery coefficient with X/W: $L/W=30$, $S/W=1$, $Q_s/Q_i=0.5$ through 1.0

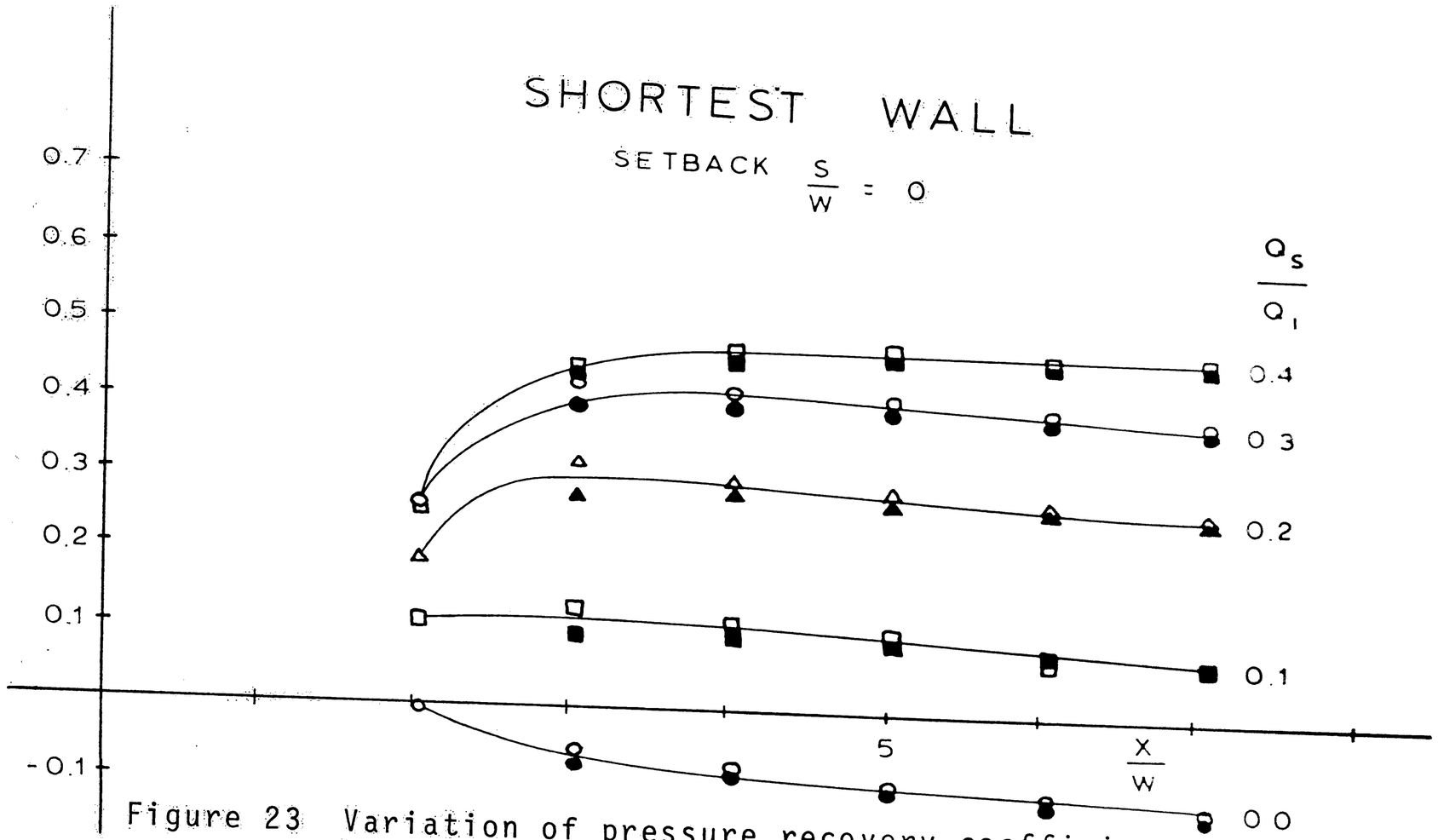

Figure 23 Variation of pressure recovery coefficient with X/W: $L/W=6$, $S/W=0$, $Q_s/Q_i=0.0$ through 0.4

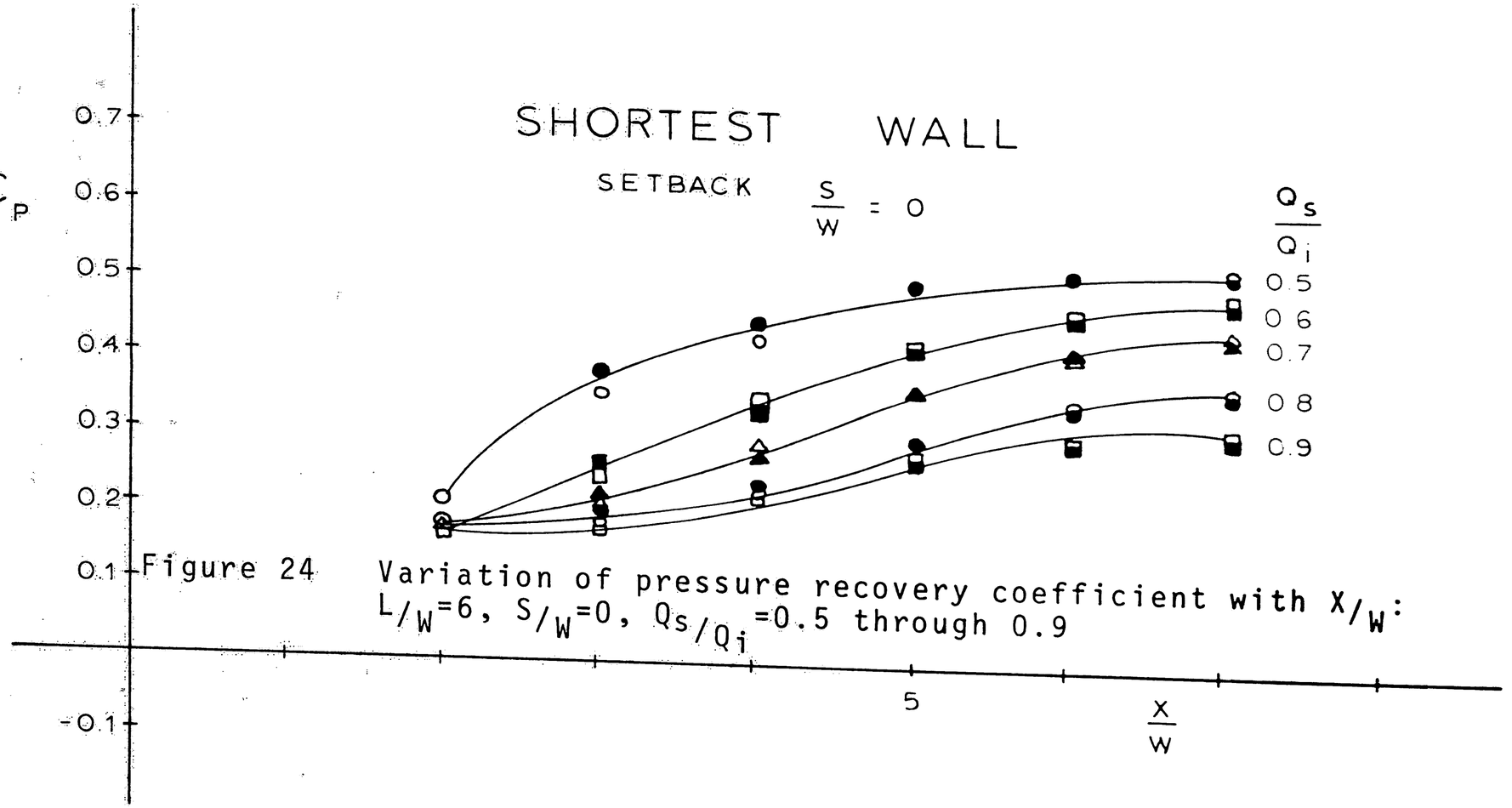

Figure 24 Variation of pressure recovery coefficient with X/W: $L/W=6$, $S/W=0$, $Qs/Qi=0.5$ through 0.9

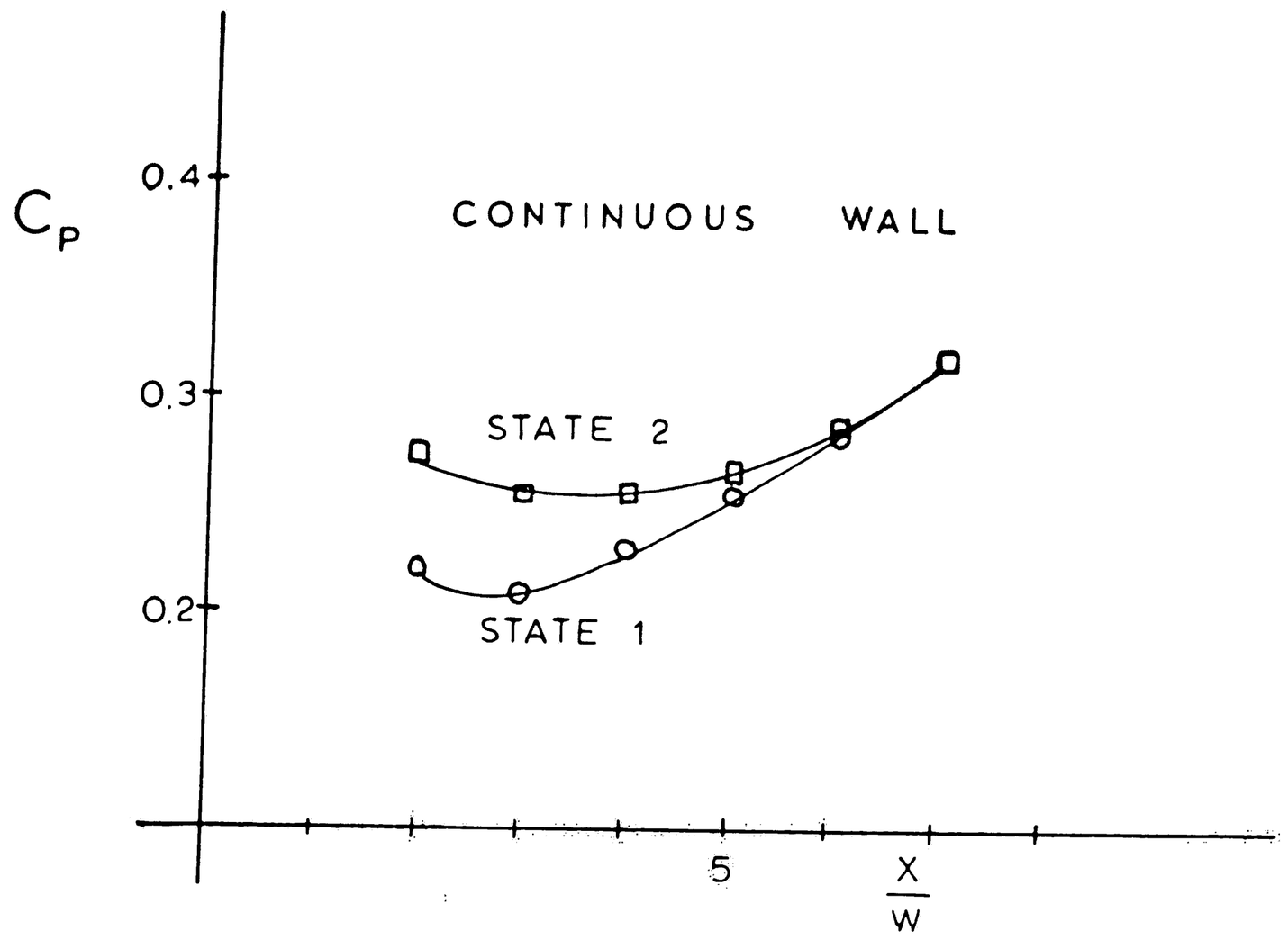

Figure 25 Two states of pressure recovery coefficient:
$L/W=6$, $S/W=0$, $Q_s/Q_i=1.0$

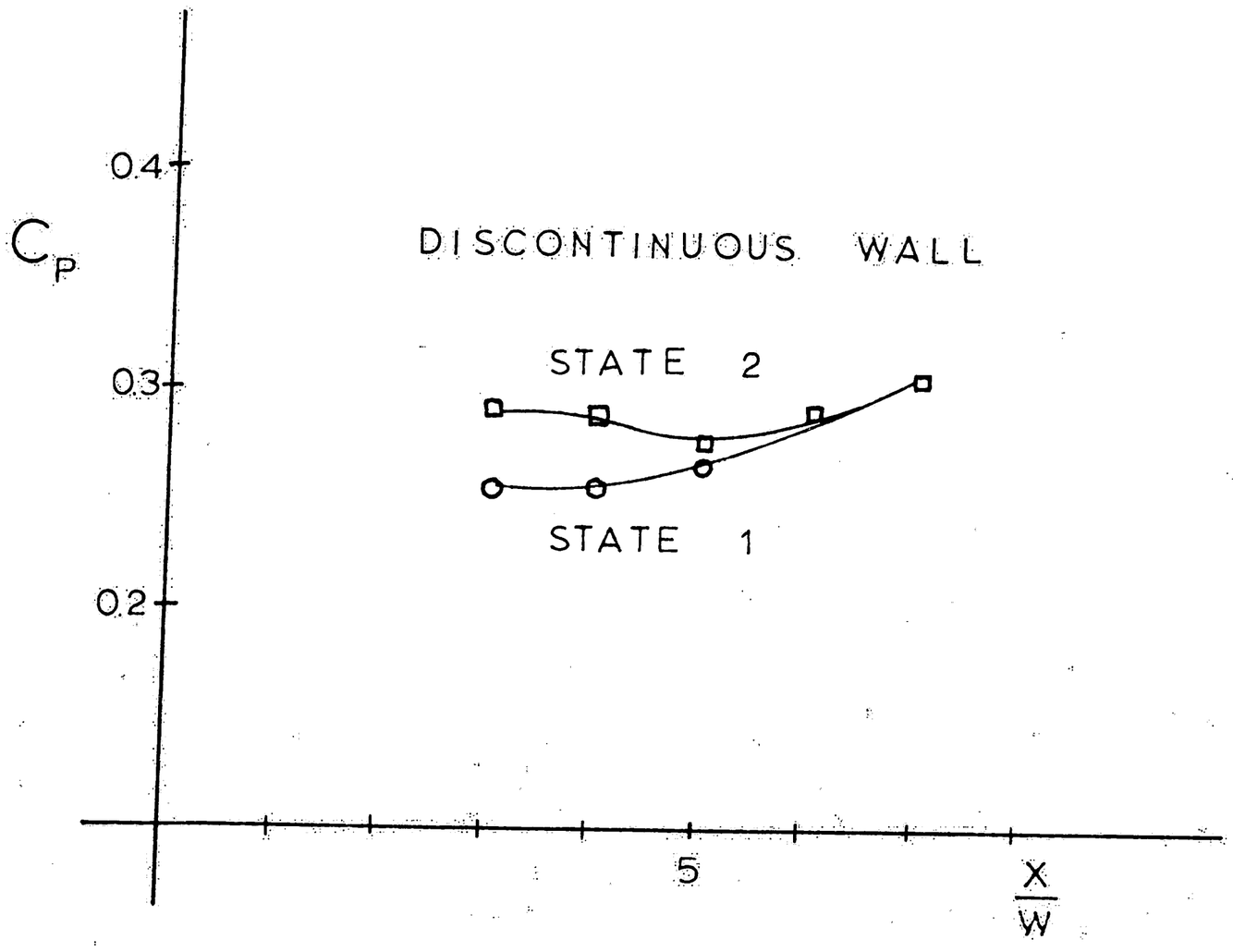

SHORTEST WALL

SETBACK $\frac{S}{W} = 1$

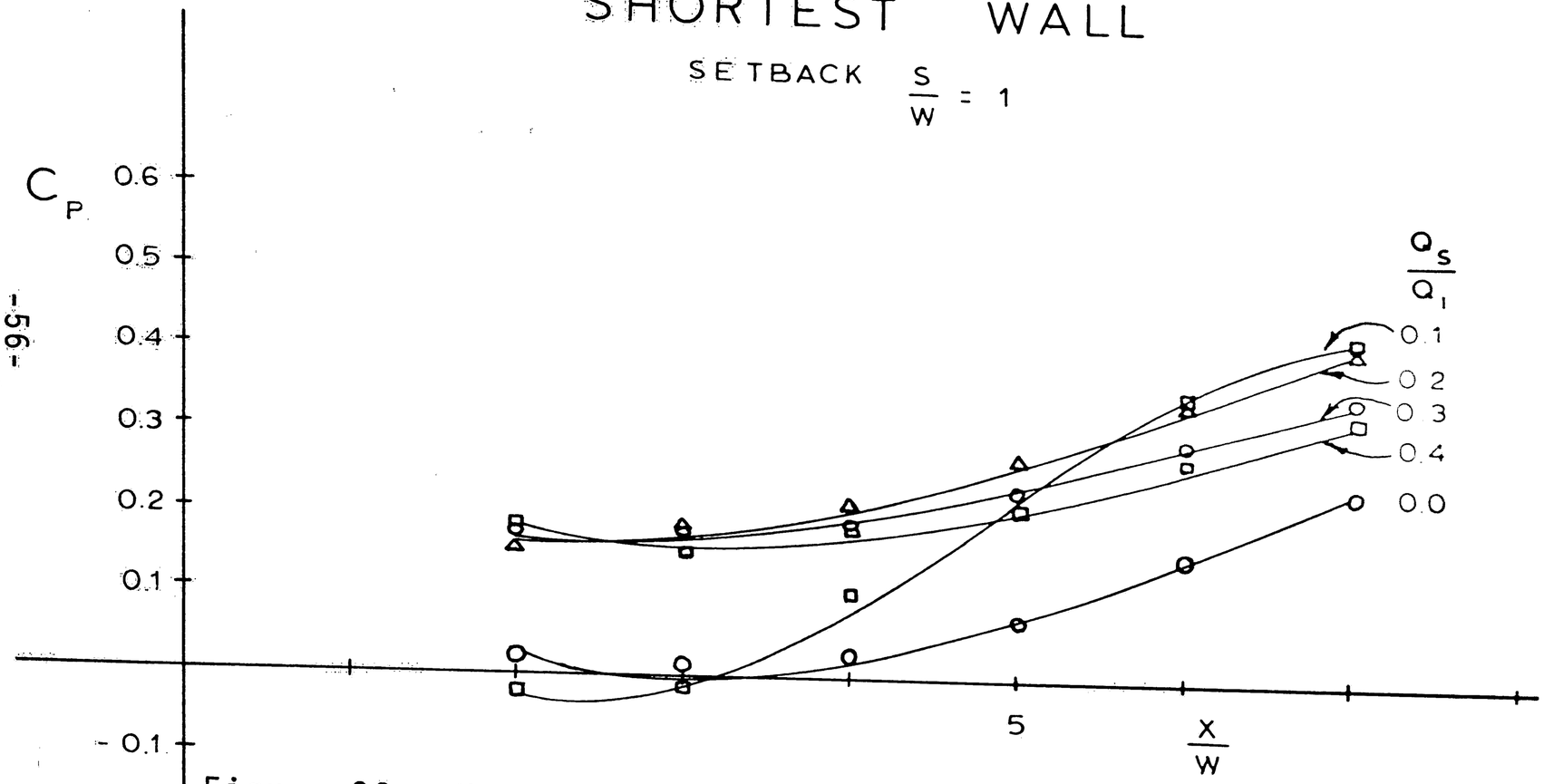

Figure 26 Variation of pressure recovery coefficient with X/W: $L/W=6$, $S/W=1$, $Q_{S/Q_i}=0.0$ through 0.4 continuous wall

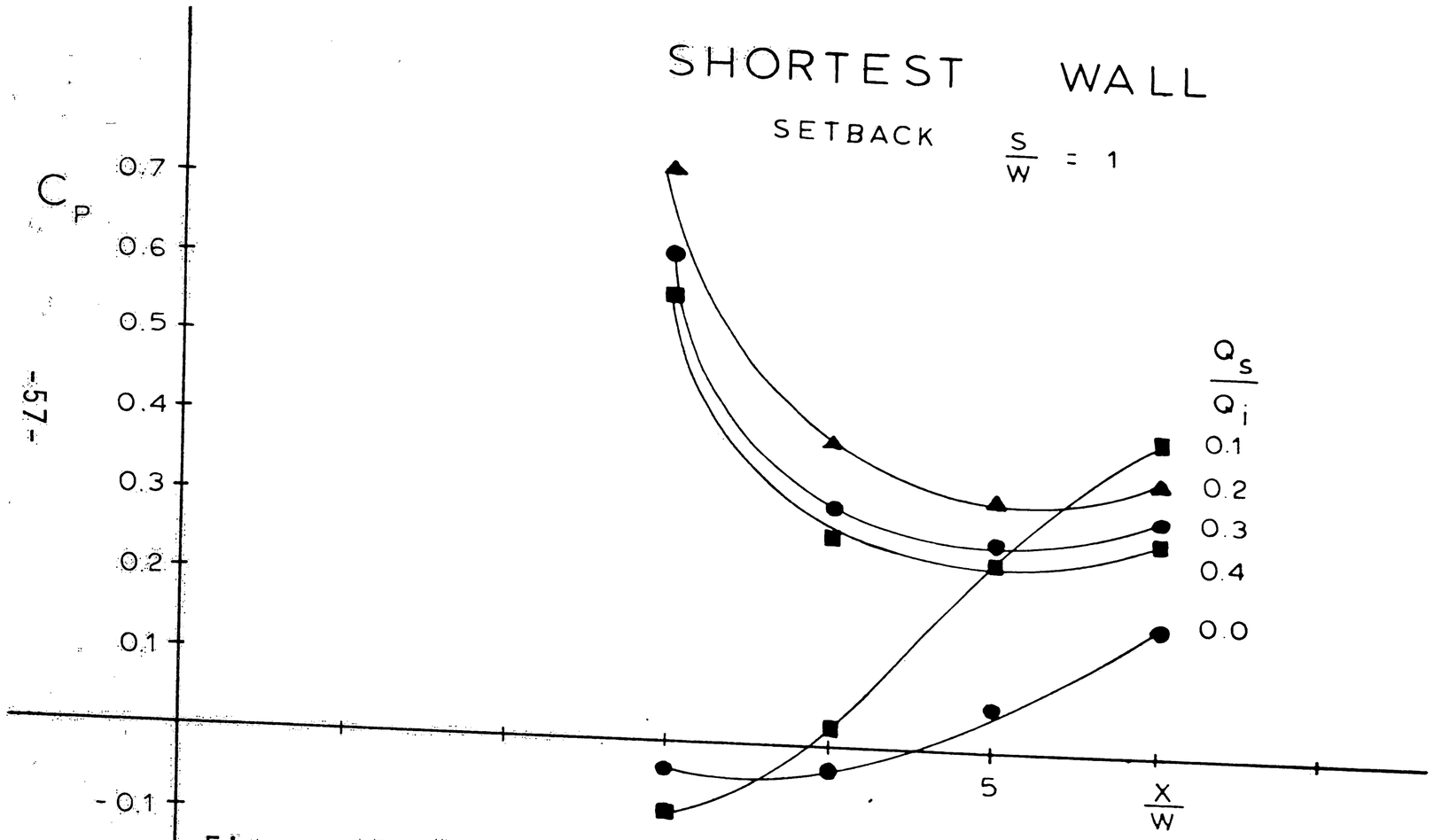

Figure 27 Variation of pressure recovery coefficient with X/W: $L/W=6$, $S/W=1$, $Q_s/Q_i=0.0$ through 0.4 discontinuous wall

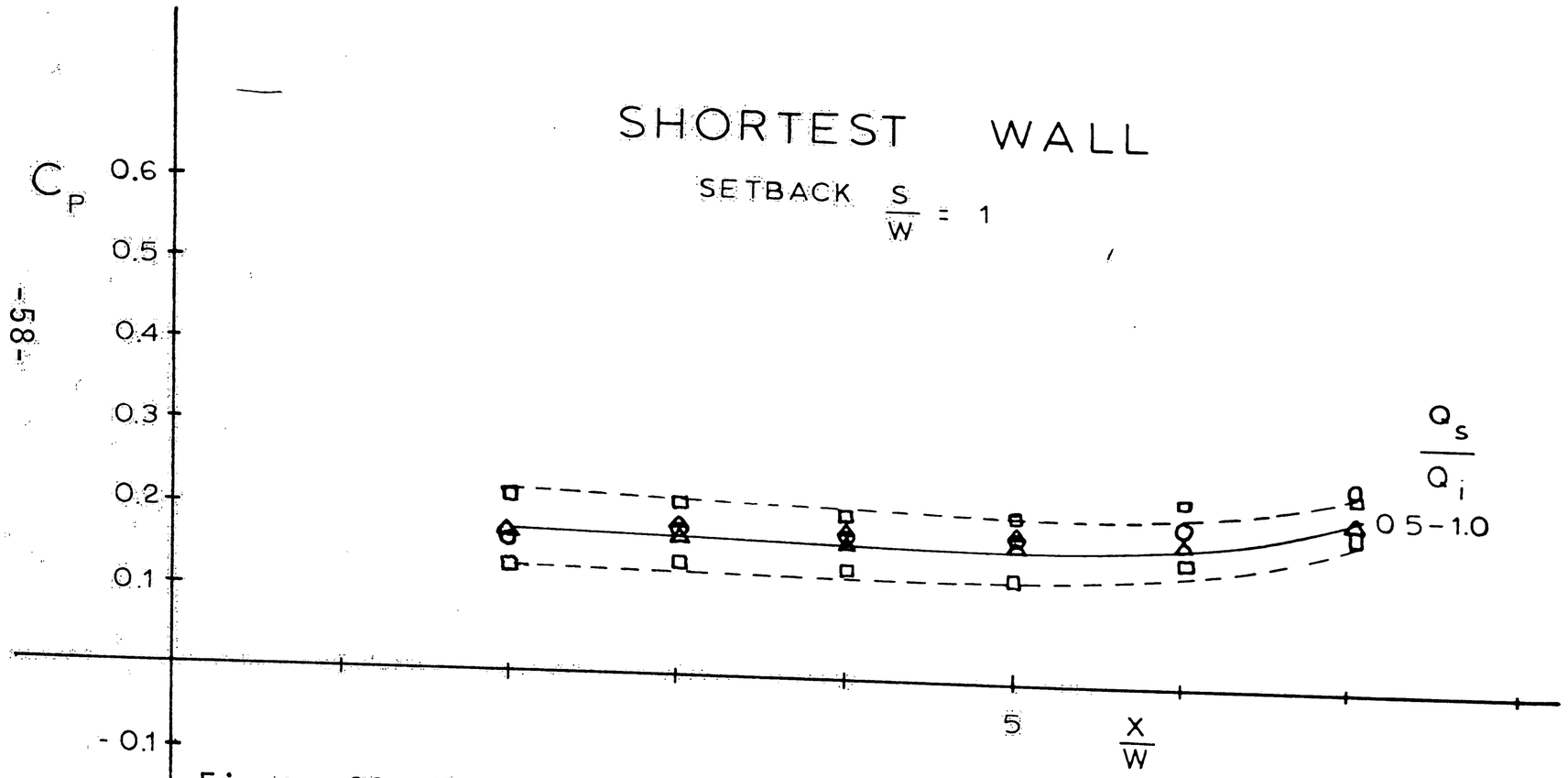

Figure 28 Variation of pressure recovery coefficient with X/W: $L/W=6$, $S/W=1$, $Q_s/Q_i=0.5$ through 1.0 continuous wall

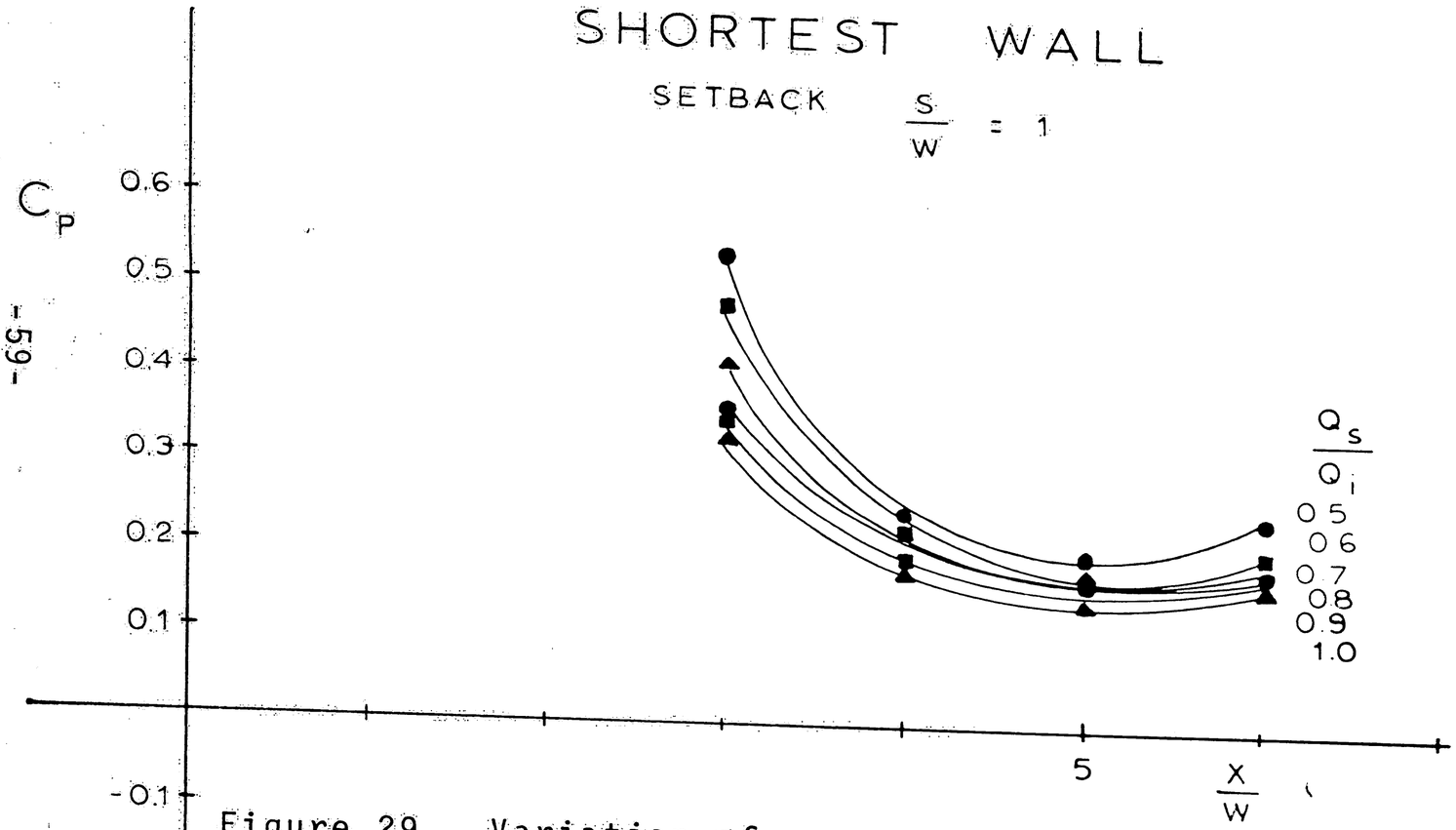

Figure 29 Variation of pressure recovery coefficient with X/W: $L/W=6$, $S/W=1$, $Q_s/Q_i=0.5$ through 1.0 discontinuous wall

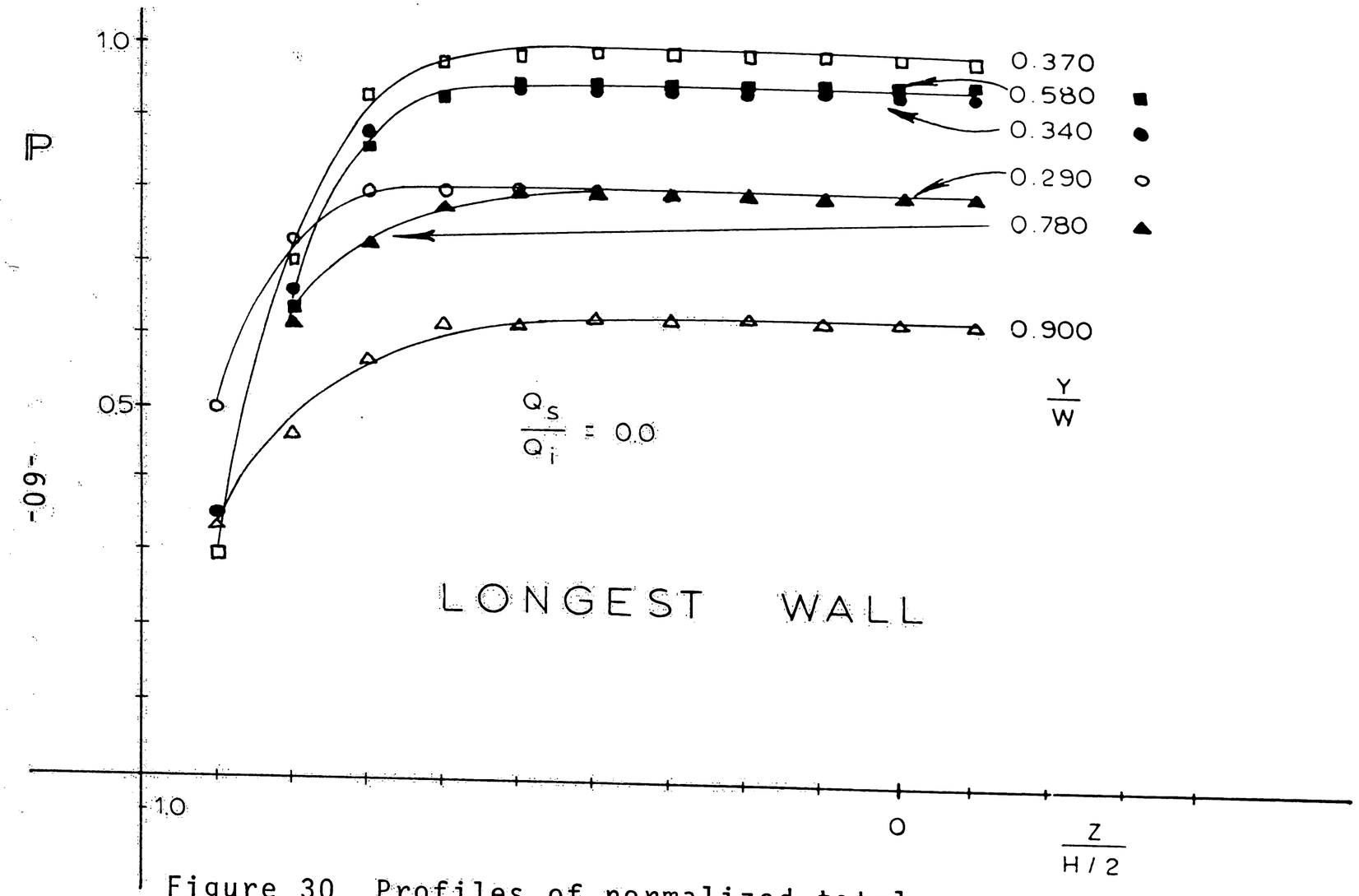

Figure 30 Profiles of normalized total pressure versus $Z/\frac{H}{2}$: $L/W=30$, $S/W=0$, $Q_s/Q_i=0.0$

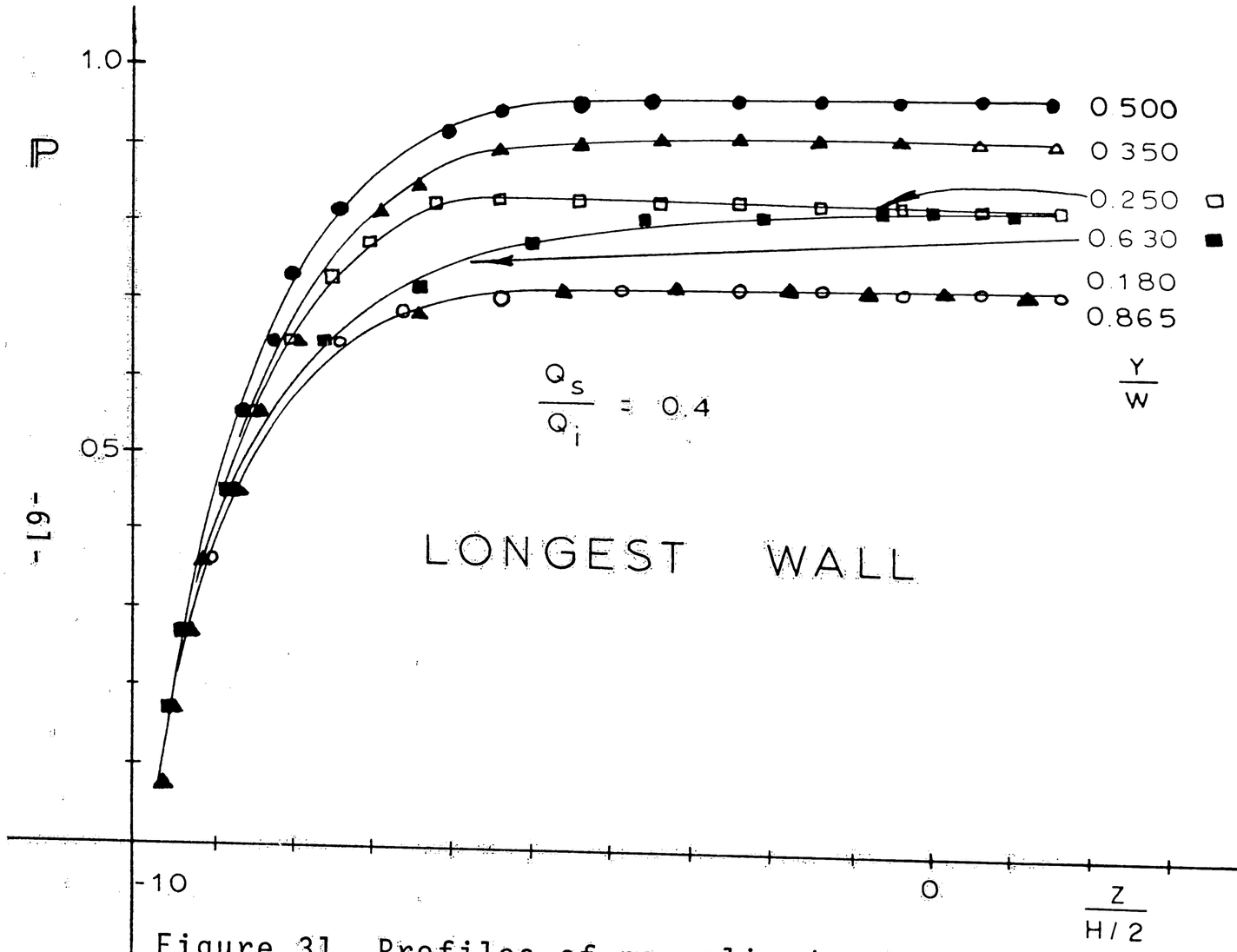

Figure 31 Profiles of normalized total pressure versus $Z/\frac{H}{2}$: $L/W=30$, $S/W=0$, $Q_{s/Q_i}=0.4$

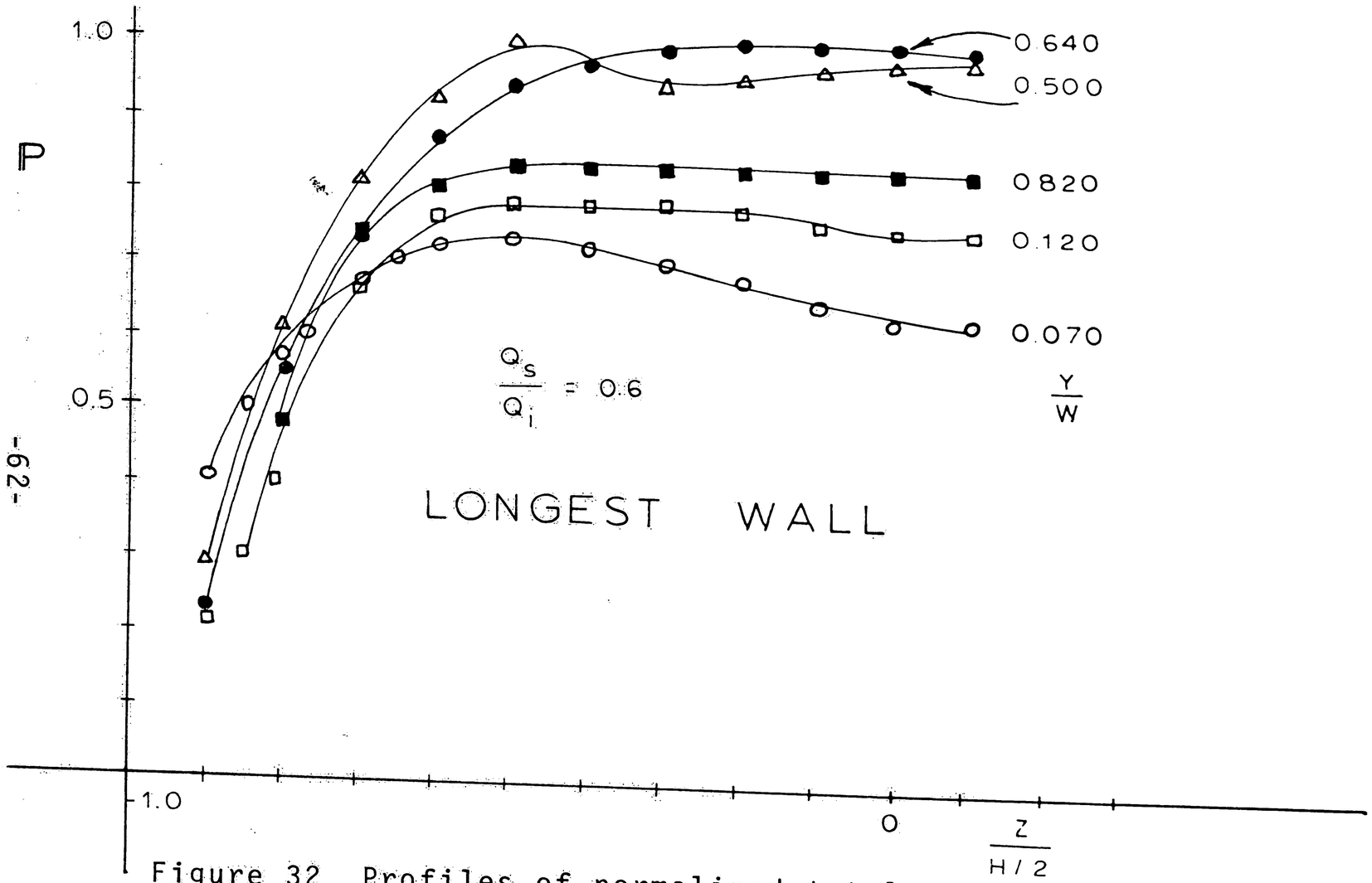

Figure 32 Profiles of normalized total pressure versus $Z/\frac{H}{2}$: $L/W=30$, $S/W=0$, $Q_s/Q_i=0.6$

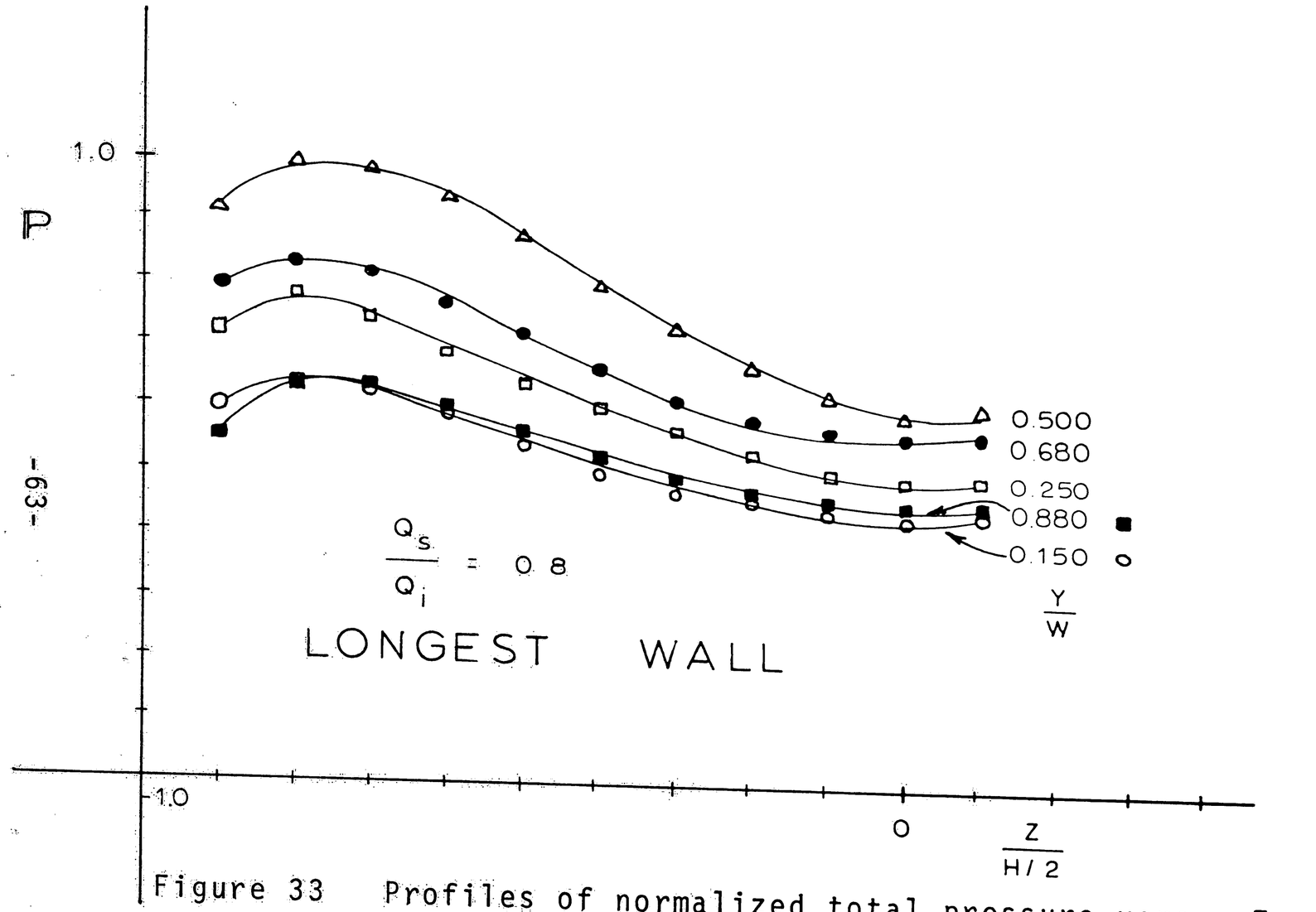

Figure 33 Profiles of normalized total pressure versus $Z/\frac{H}{2}$: $L/W=30$, $S/W=0$, $Q_s/Q_i=0.8$

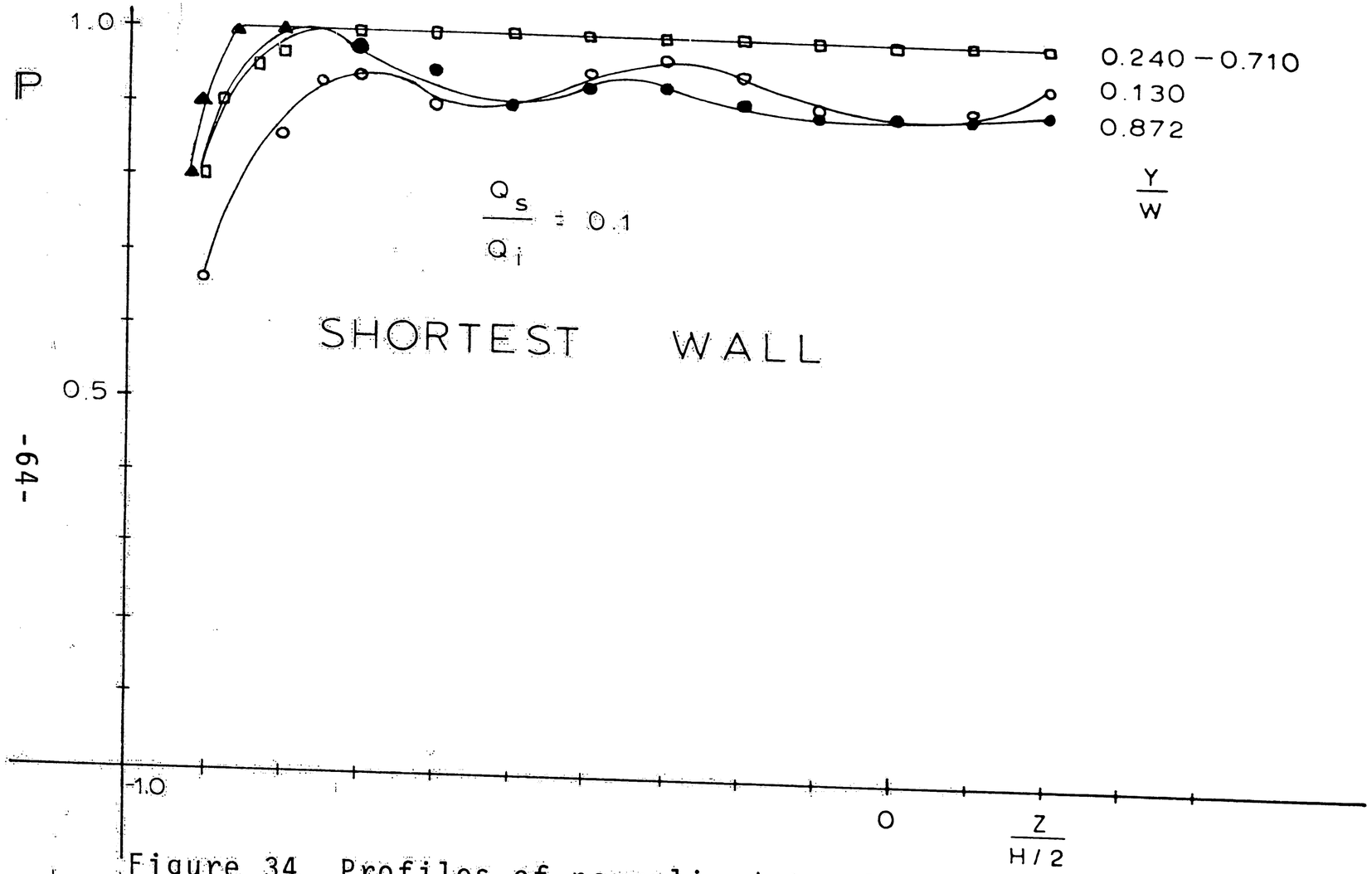

Figure 34 Profiles of normalized total pressure versus $Z/\frac{H}{2}$: $L/W=6$, $S/W=0$, $Q_s/Q_i=0.1$

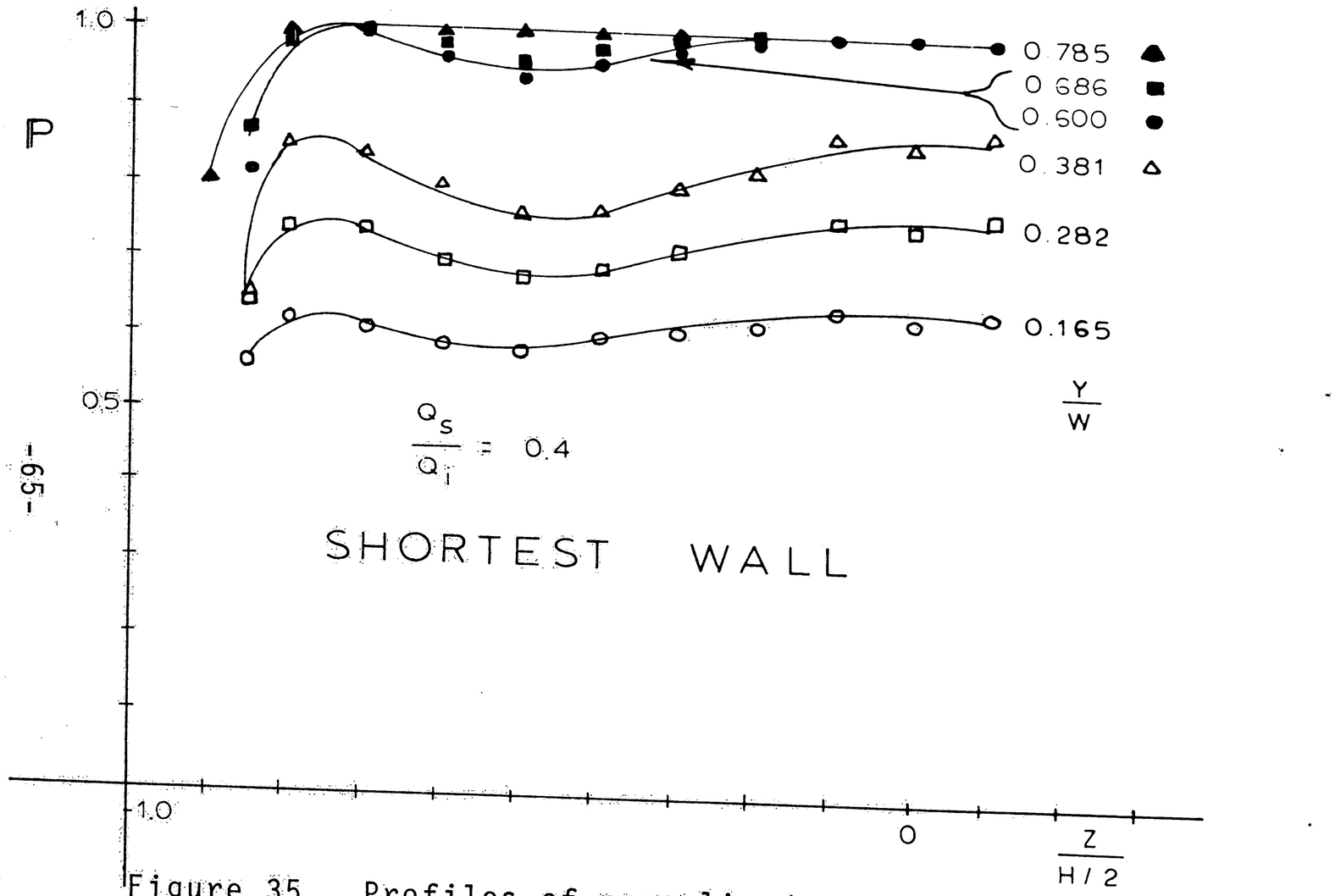

Figure 35 Profiles of normalized total pressure versus $Z/\frac{H}{2}$: $L/W=6$, $S/W=0$, $Q_s/Q_i=0.4$

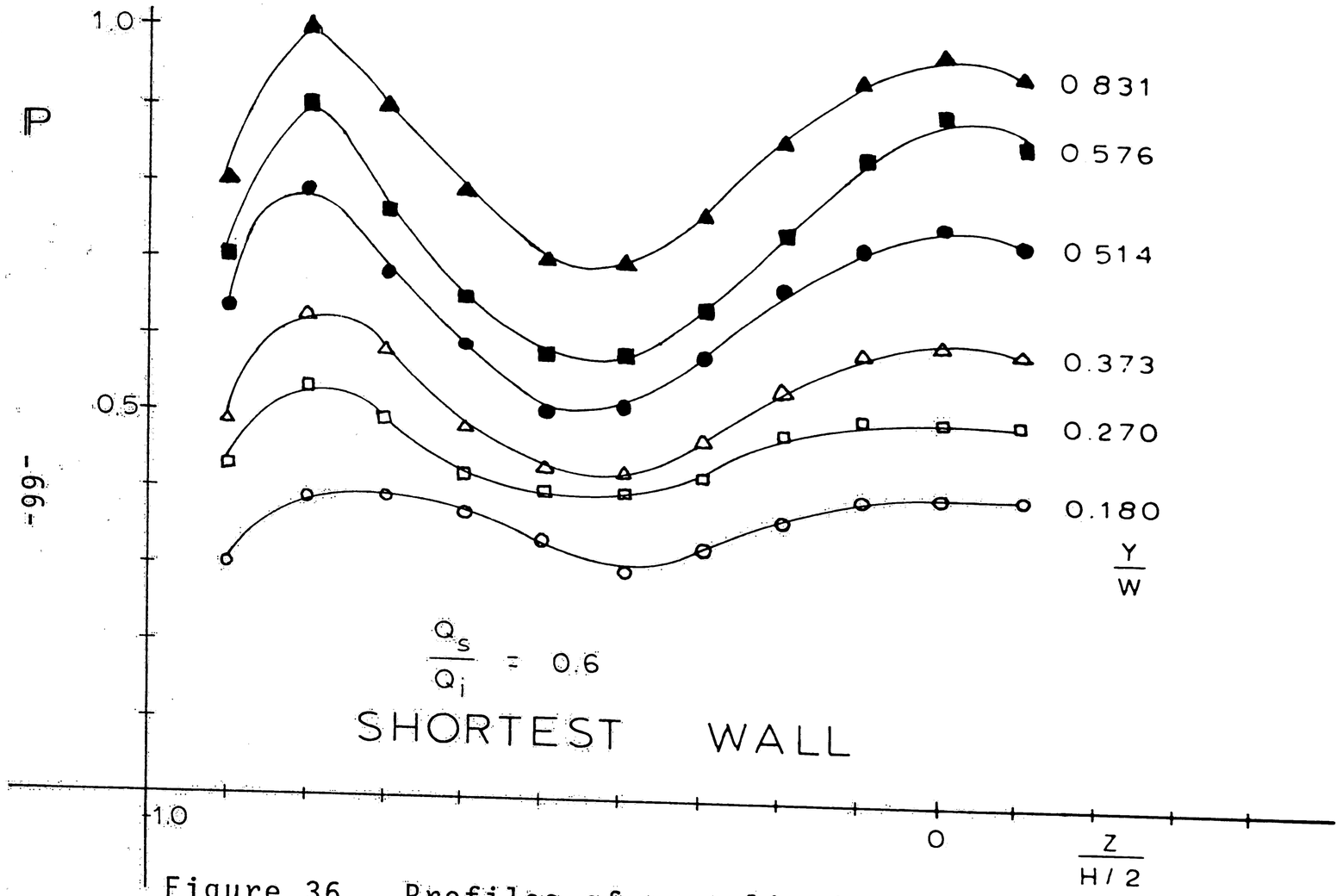

Figure 36 Profiles of normalized total pressure versus $Z/\frac{H}{2}$: $L/W=6$, $S/W=0$, $Q_s/Q_i=0.6$

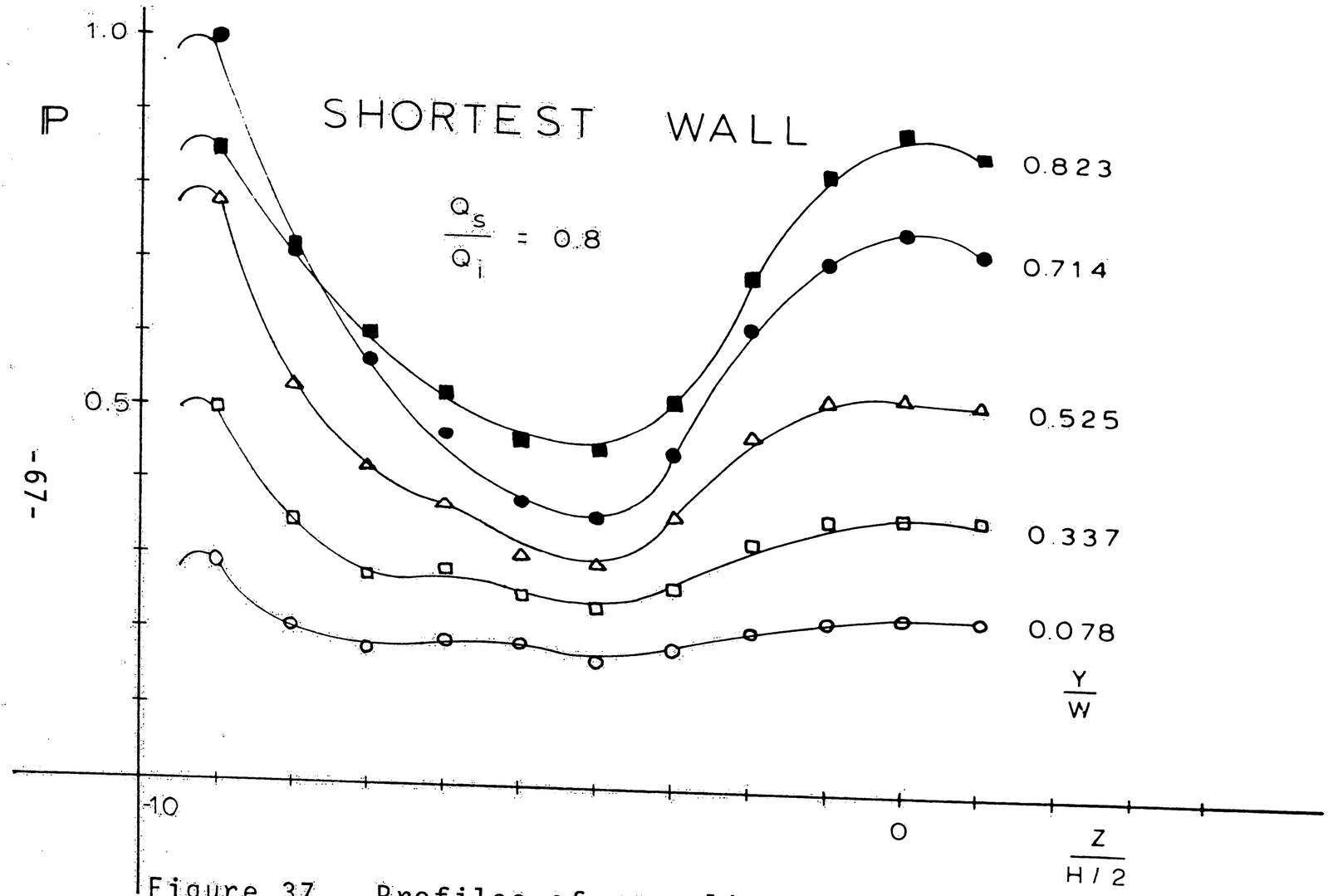

Figure 37 Profiles of normalized total pressure versus $Z/\frac{H}{2}$: $L/W=6$, $S/W=0$, $Q_s/Q_i=0.8$

SHORTEST WALL

$\frac{Q_s}{Q_i} = 0.6$

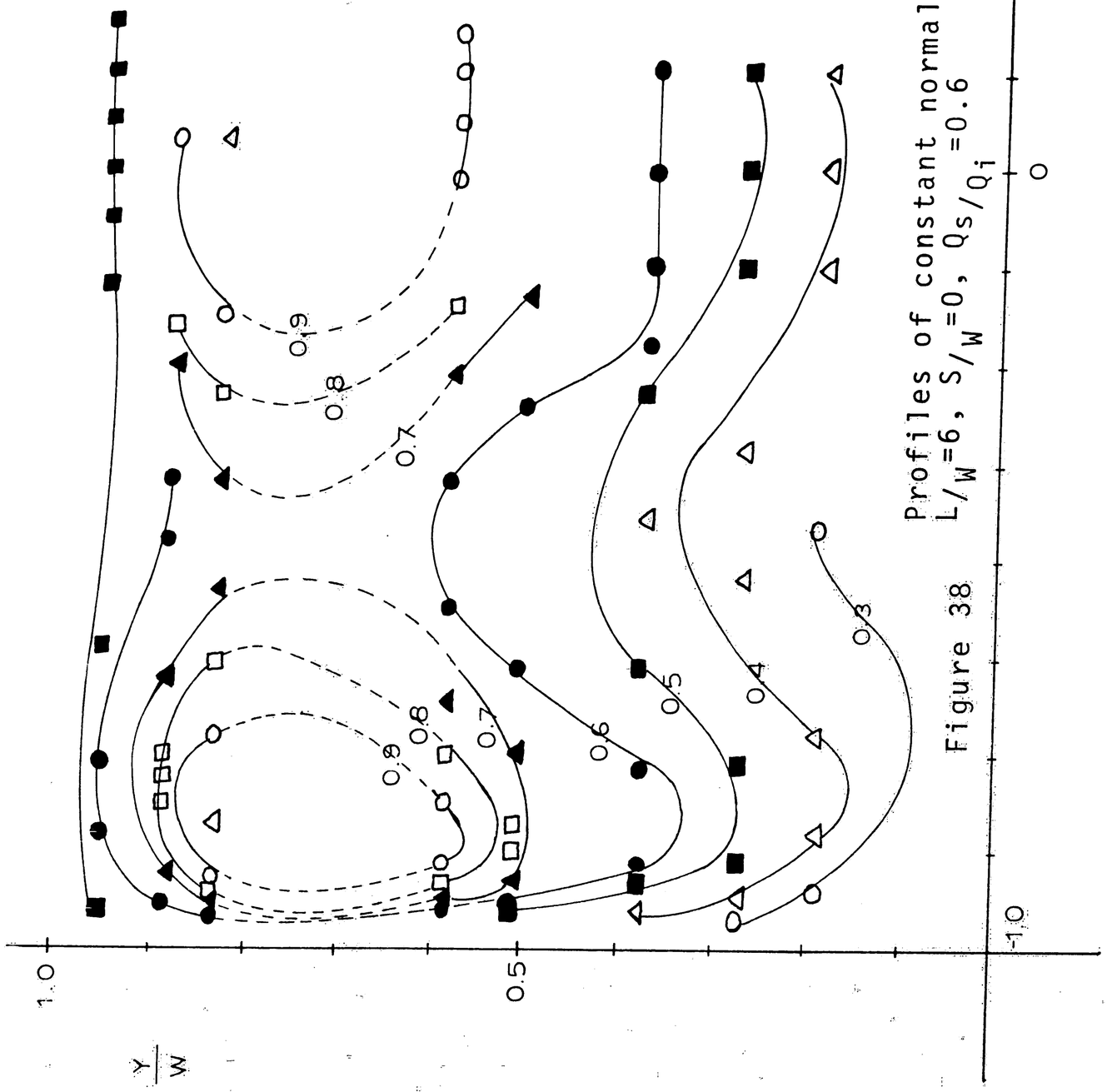

Figure 38 Profiles of constant normalized total pressure: $L/W=6$, $S/W=0$, $Q_s/Q_i=0.6$

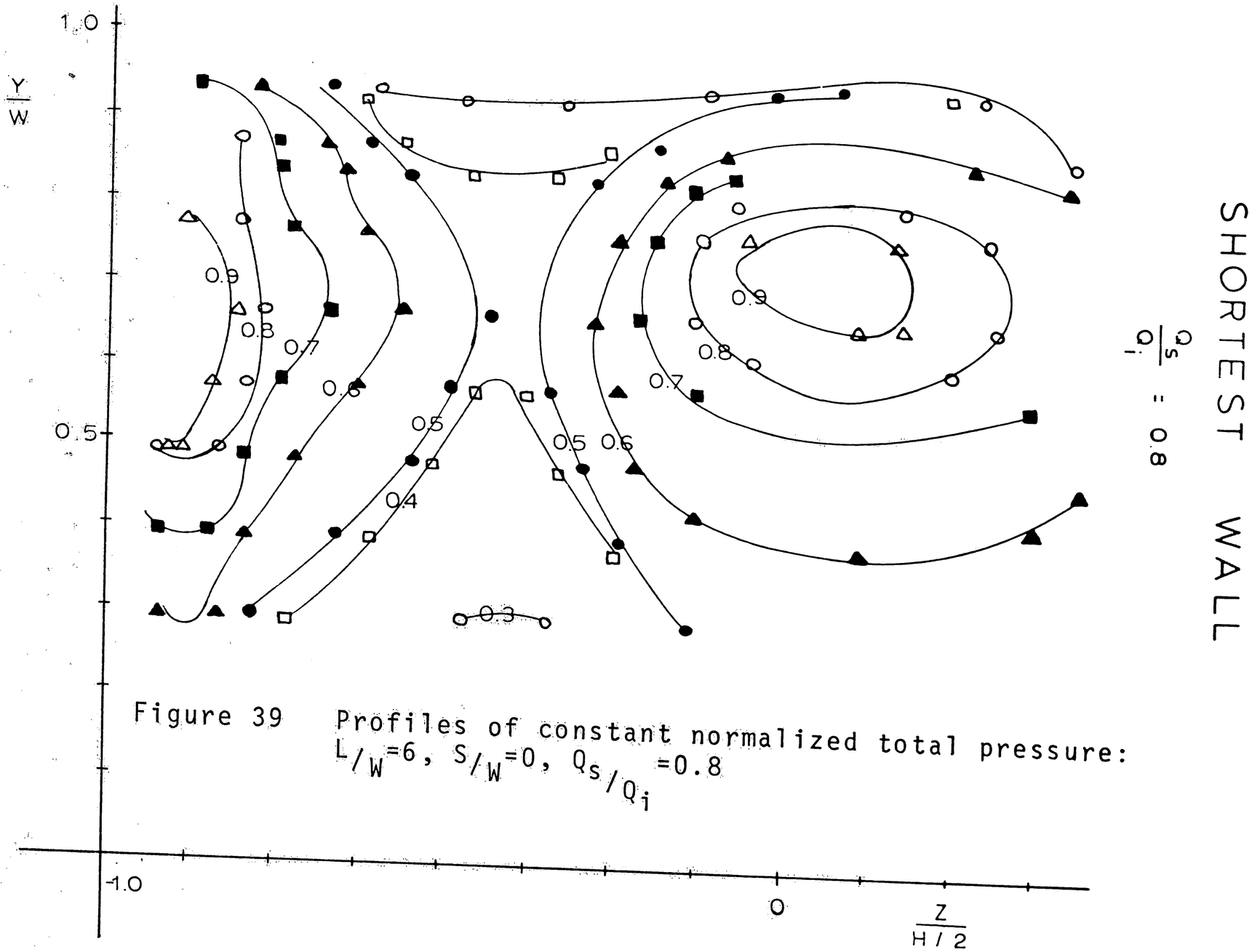

Figure 39 Profiles of constant normalized total pressure: $L/W=6$, $S/W=0$, $Q_s/Q_i=0.8$

Vita

The son of Mr. and Mrs. John E. Bach, Stephen John Bach, was born on November 9, 1949, in Jamaica, New York. He attended high school in New Hyde Park, New York, and graduated in 1967. In the fall of that year, he entered Lehigh University and received a Bachelor of Science degree in Mechanical Engineering in June of 1971.

He remained at Lehigh University as a graduate student in the Department of Mechanical Engineering.